Advances in Imaging Brain Metabolism

Fahmeed Hyder and Douglas L. Rothman

Department of Biomedical Engineering, Department of Radiology and Biomedical Imaging, Magnetic Resonance Research Center, and Quantitative Neuroscience with Magnetic Resonance Core Center, Yale University, New Haven, Connecticut 06520; email: fahmeed.hyder@yale.edu

Annu. Rev. Biomed. Eng. 2017. 19:485–515

The *Annual Review of Biomedical Engineering* is online at bioeng.annualreviews.org

https://doi.org/10.1146/annurev-bioeng-071516-044450

Keywords

aerobic glycolysis, excitation, inhibition, glycogen, oxidative phosphorylation, neuroimaging

Abstract

Metabolism is central to neuroimaging because it can reveal pathways by which neuronal and glial cells use nutrients to fuel their growth and function. We focus on advanced magnetic resonance imaging (MRI) and magnetic resonance spectroscopy (MRS) methods used in brain metabolic studies. ^{17}O-MRS and ^{31}P-MRS, respectively, provide rates of oxygen use and ATP synthesis inside mitochondria, whereas ^{19}F-MRS enables measurement of cytosolic glucose metabolism. Calibrated functional MRI (fMRI), an advanced form of fMRI that uses contrast generated by deoxyhemoglobin, provides maps of oxygen use that track neuronal firing across brain regions. ^{13}C-MRS is the only noninvasive method of measuring both glutamatergic neurotransmission and cell-specific energetics with signaling and nonsignaling purposes. Novel MRI contrasts, arising from endogenous diamagnetic agents and exogenous paramagnetic agents, permit pH imaging of glioma. Overall, these magnetic resonance methods for imaging brain metabolism demonstrate translational potential to better understand brain disorders and guide diagnosis and treatment.

Contents

1. INTRODUCTION 486
2. FROM PROTONS TO NEURONS TO METABOLISM 487
   2.1. A Primer on Magnetic Resonance 487
   2.2. A Primer on Neural Activity 488
   2.3. A Primer on Brain Metabolism 492
3. IMAGING NEUROENERGETICS AND NEUROTRANSMISSION 493
   3.1. ^{13}C-MRS for Tricarboxylic Acid Cycle Flux 493
   3.2. ^{13}C-MRS for Glutamate Neurotransmitter Flux 495
   3.3. Energetics of Signaling and Nonsignaling Components 495
4. IMAGING METABOLIC DEMAND OF RESTING ACTIVITY 496
   4.1. ^{31}P-MRS for Rate of ATP Production 496
   4.2. ^{17}O-MRS and ^{19}F-MRS for Oxygen and Glucose Consumption 497
5. IMAGING METABOLIC DEMAND OF STIMULATED ACTIVITY 499
   5.1. Metabolic Demands of Neural Hemodynamic–Associated and –Disassociated Areas 500
   5.2. Metabolic Interactions Between Resting and Stimulated Activities 501
6. NOVEL METHODS FOR MOLECULAR IMAGING OF CANCER 501
   6.1. Intratumoral pH-Weighted Imaging 504
   6.2. Intratumoral and Peritumoral pH Imaging 505
7. CONCLUDING REMARKS AND FUTURE PERSPECTIVES 508

1. INTRODUCTION

The complexity of the human brain is often described in terms of its anatomy. The brain consists of an enormous number of neurons and glial cells (1) making elaborate synapses that are both chemical and electrical (2) and that, together, enable us to perceive a range of sensations and be conscious. Neuroscience has traditionally separated structural and functional studies of the brain (3), but metabolism is the common thread that connects these apparently disparate areas of neuroscientific enquiry (4). Catabolic reactions help cells release energy to support multiple functions (e.g., action potential generation and propagation, synaptic transmission, neurotransmitter recycling, calcium activities) that allow cells to communicate with one another (5, 6), whereas anabolic pathways supply the fuel needed to (re)build cellular structures and/or store as energy reserves for later use (7).

Thus, metabolism is central to our understanding of how the brain's anatomy and physiology change with aging, disease, and/or injury. The basic question of how much fuel is used for cellular building blocks versus cellular functional activity is fundamental for quantitative functional imaging of the brain, specifically because the energy demands of normal brain function are very high (8). But this same question is also relevant to molecular imaging of brain disorders, especially cancer because it is a disease of uncontrolled cell growth, which requires metabolism of fuel (9).

The anatomical and physiological complexities of the brain are studied with an impressive arsenal of biomedical imaging tools, ranging from translational methods such as magnetic resonance imaging (MRI), magnetic resonance spectroscopy (MRS), and positron emission tomography (PET), which are used in both preclinical and clinical research, to electrophysiological and optical imaging methods, which are used primarily in basic science research (**Figure 1*a***). However, a unique property of magnetic resonance versus other methods is its ability to safely, noninvasively,

and reproducibly map the human brain's structure and activity at sufficiently high spatial resolution to enable the study of changes in both gray and white matter on various temporally dynamic scales (10, 11).

If one is interested in how cells work, what their main nutrients are, how they get the nutrients, how they use nutrients to support growth and function, and how they eventually malfunction, then one needs specific in vivo MRI and MRS techniques that quantitatively measure cerebral metabolism. In addition to the prominence of functional MRI (fMRI) in neuroscience (12), many MRI and MRS methods for imaging brain metabolism are being used in an attempt to answer these questions and are having an important and lasting impact on translational neuroscience (13). Many of these types of metabolic scans from MRI and MRS can even be combined with anatomical MRI scans to provide insights into differences between health and disease (14).

2. FROM PROTONS TO NEURONS TO METABOLISM

In this section, we provide some background on magnetic resonance (15, 16), activities at the nerve terminal (3, 16), and cerebral metabolism (4, 16).

2.1. A Primer on Magnetic Resonance

Nuclei containing odd numbers of protons or neutrons have an intrinsic magnetic moment in the presence of a strong static magnetic field (B_o). Typical B_o values for in vivo rat and human experiments, respectively, are 7.0 T (or higher) and 3.0 T; higher B_o values lead to a higher signal-to-noise ratio (SNR). Some biologically relevant nonradioactive isotopes are ^{1}H, ^{13}C, ^{15}N, ^{17}O, ^{19}F, ^{23}Na, and ^{31}P. Sensitivity for an isotope depends on the gyromagnetic ratio and the natural abundance (**Table 1**). With ^{1}H, for instance, the main distinction between MRI and MRS methods is that the exquisite spatial resolution in MRI is due to the strong ^{1}H signal from high water/fat content in soft tissues (**Figure 1*b***), whereas the superior molecular information offered by MRS comes from the dilute ^{1}H signal from molecules other than water/fat (**Figure 1*c***).

Most MRI methods rely on the transverse relaxation rate (R_2^* by gradient echo or R_2 by spin echo) and longitudinal relaxation rate (R_1) of tissue water–^{1}H to map both structure and function (**Figure 1*b***). All of these MRI contrasts enable good visualization of tissue anatomy, but diffusion-weighted MRI, which maps the extent of the Brownian motion of tissue water–^{1}H, allows exquisite depiction of white matter anatomy (10, 12). Examples of functional scans include blood oxygenation level–dependent (BOLD), cerebral blood flow (CBF), and cerebral blood volume (CBV). CBF is measured by radio-frequency (RF) labeling of blood water–^{1}H that, upon mixing with tissue water–^{1}H, alters the R_1 (17). Contrasts such as BOLD (18) and CBV (19) are reflected by magnetic susceptibility contrast induced by paramagnetic deoxyhemoglobin and superparamagnetic iron oxide (SPIO) nanoparticles within the blood, where intravascular magnetic fields affect the R_2^* and/or R_2 of tissue water–^{1}H. Multimodal BOLD, CBV, and CBF scans are crucial for calibrated fMRI (see Section 5).

MRS uses differences in resonance frequency between dissimilar chemical groups to measure the regional concentrations of endogenous molecules, including lactate, glucose, glutamate, γ-aminobutyric acid (GABA), glutathione, and glutamine (15, 16). MRS data can also be viewed in two or three dimensions with chemical shift imaging (CSI), but the images are not as crisp as MRI data because the voxels are much larger (**Figure 1*c***). ^{13}C-MRS, in combination with infusion of ^{13}C-labeled substrates such as glucose or acetate, enables detection of the rates of ^{13}C-label incorporation into cell-specific pools (e.g., glutamate and GABA are predominantly neuronal, whereas glutamine is predominantly glial) (see Section 3). A range of MRS and MRI methods provide other metabolic measurements (see Sections 4 and 6).

2.2. A Primer on Neural Activity

The integrity of brain function is maintained by electrical communication among neurons in an active partnership with astrocytes, where cytological association with the microvasculature (**Figure 2*a***) provides the framework that links activities at the nerve terminal to energy demand and blood flow (20). Glutamate is the major excitatory neurotransmitter, and GABA is its conjugate inhibitory partner; together, they constitute ~90% of cortical neurons (21). Glutamate metabolism

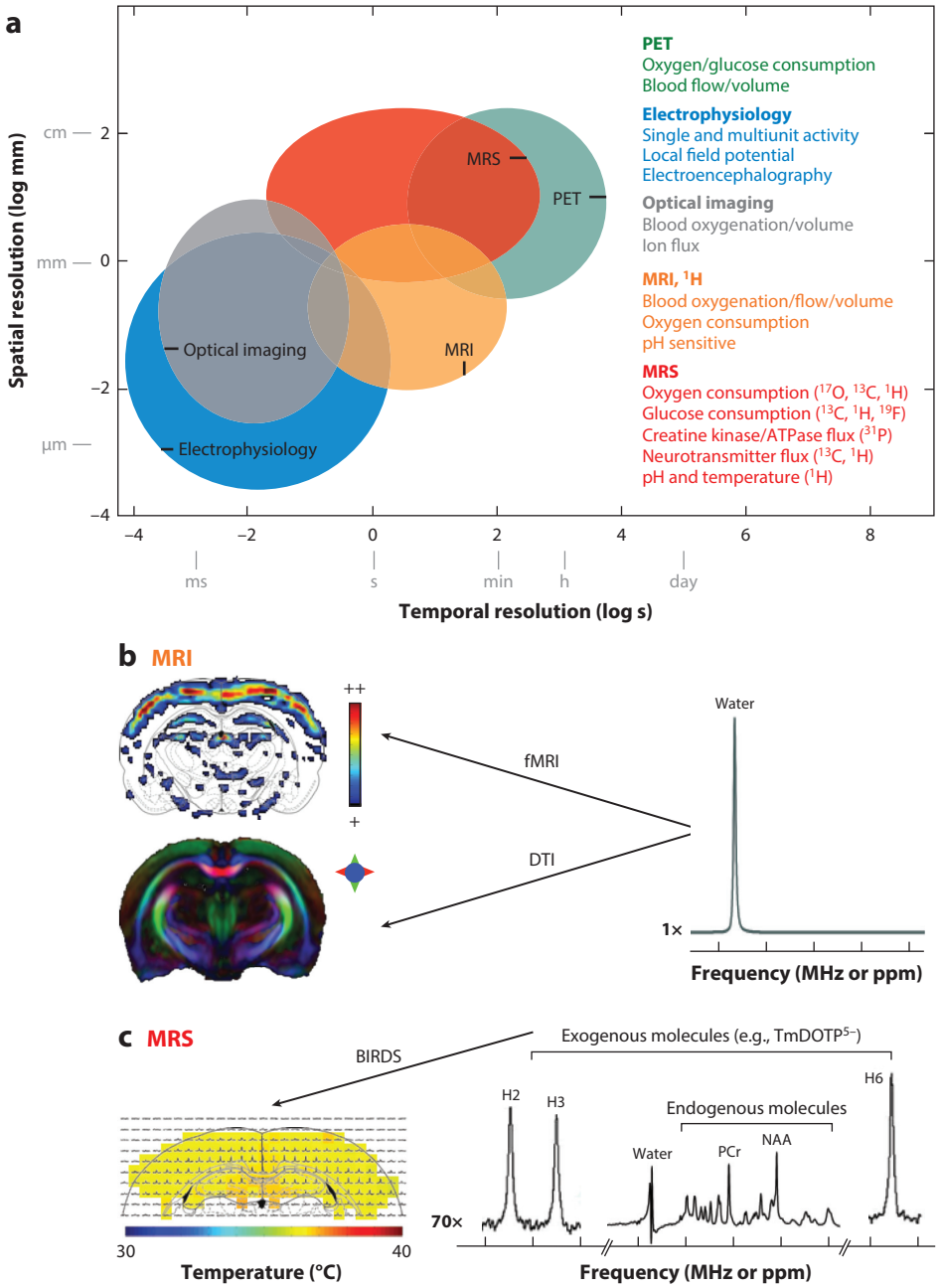

Table 1 Physical properties of various nuclei used in metabolic measurements by MRI and MRS methods[a]

Isotope (spin)	Natural abundance (%)	Gyromagnetic ratio [10^6 rad/(s·T)]	Frequency (500 MHz)	Metabolic measurement			
				by MRS (voxel size)	Section of text	by MRI (voxel size)	Section of text
^{1}H (1/2)	~100	267.522	−500.00	$CMR_{glc(ox)}$ (~20 mm^3)	3	CMR_{O2} (~0.5 mm^3)	5
				V_{cycle} (~20 mm^3)	3		
				pH (~2 mm^3)	6	pH (~0.5 mm^3)	6
^{13}C (1/2)	1.1	67.238	−125.725	$CMR_{glc(ox)}$ (~100 mm^3)	3		
				V_{cycle} (~100 mm^3)	3		
^{17}O (5/2)	0.04	−36.281	67.782	CMR_{O2} (~15 mm^3)	4		
^{19}F (1/2)	~100	251.815	−470.47	CMR_{glc} (~60 mm^3)	4		
^{31}P (1/2)	~100	108.394	−202.606	CMR_{ATPase} (~15 mm^3)	4		
				CMR_{CK} (~15 mm^3)	4		

[a]The spatial resolution indicated for rat brain at a magnetic field (B_o) of ≥9.4 T; substituting the units of cubic millimeters with cubic centimeters roughly approximates the spatial resolution observed in human brain at a B_o value of ≥4.0 T. Abbreviations: CMR_{ATPase}, cerebral metabolic rate of ATPase reaction; CMR_{CK}, cerebral metabolic rate of creatine kinase reaction; CMR_{glc}, cerebral metabolic rate of glucose consumption; $CMR_{glc(ox)}$, cerebral metabolic rate of glucose oxidation; CMR_{O2}, cerebral metabolic rate of oxygen consumption; MRI, magnetic resonance imaging; MRS, magnetic resonance spectroscopy; V_{cycle}, total neurotransmitter cycle flux.

Figure 1

Metabolic methods used in neuroimaging. (*a*) Spatial resolution (*vertical axis*) and temporal resolution (*horizontal axis*) of different methods, such as electrophysiology, optical imaging, positron emission tomography (PET), magnetic resonance imaging (MRI), and magnetic resonance spectroscopy (MRS). Each method measures different tissue- and/or cell-specific components and has specific advantages and disadvantages. Because demand for energy substrates is a fundamental requirement, energy-based methods enable quantitative neuroimaging. (*b*) MRI measures both brain function [e.g., functional MRI (fMRI)] and brain anatomy [e.g., diffusion tensor imaging (DTI)] with high spatial resolution because of the concentrated water–^{1}H signal (~50 M). (*Top*) fMRI and (*bottom*) DTI maps (from a rat brain) are measured by relaxation and diffusion rates, respectively, of water. (*c*) MRS measures dilute ^{1}H signals (0.5–5 mM) from molecules other than water (or fat) for molecular imaging [i.e., biosensor imaging of redundant deviation in shifts (BIRDS)]. MRS detects endogenous [e.g., phosphocreatine (PCr), *N*-acetyl aspartate (NAA)] or exogenous [e.g., thulium chelated with 1,4,7,10-tetraazacyclododecane-1,4,7,10-tetrakis(methylene phosphonate) ($TmDOTP^{5-}$)] molecules. Diamagnetic endogenous ^{1}H signals such as water, NAA, and PCr span a chemical shift range of ~5 ppm, whereas chemical shifts of paramagnetic exogenous ^{1}H signals from $TmDOTP^{5-}$ span more than 200 ppm. Because these chemical shifts describe the molecule's structure in relation to its environment, they can be used for highly specific molecular imaging, such as a temperature map (from a rat brain) generated from chemical shift imaging of the ^{1}H signals from $TmDOTP^{5-}$ (see Section 6.2).

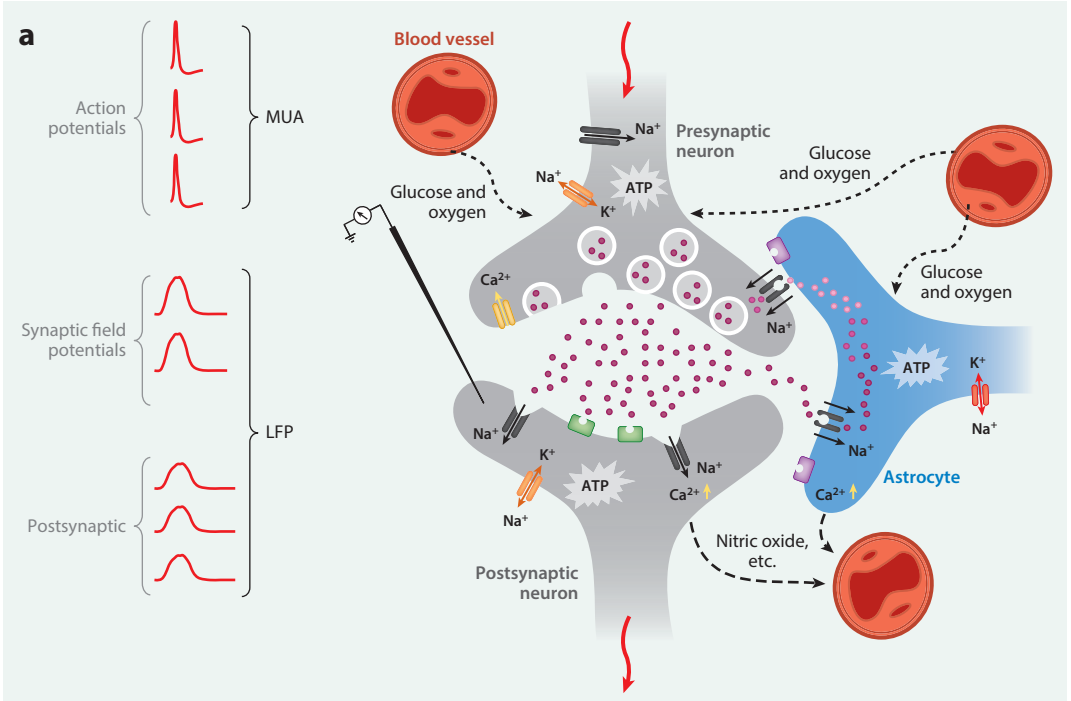
a
Action potentials
MUA
Synaptic field potentials
LFP
Postsynaptic
Blood vessel
Glucose and oxygen
Presynaptic neuron
Na+
K+
ATP
Ca2+
Glucose and oxygen
Glucose and oxygen
Astrocyte
Nitric oxide, etc.
Postsynaptic neuron

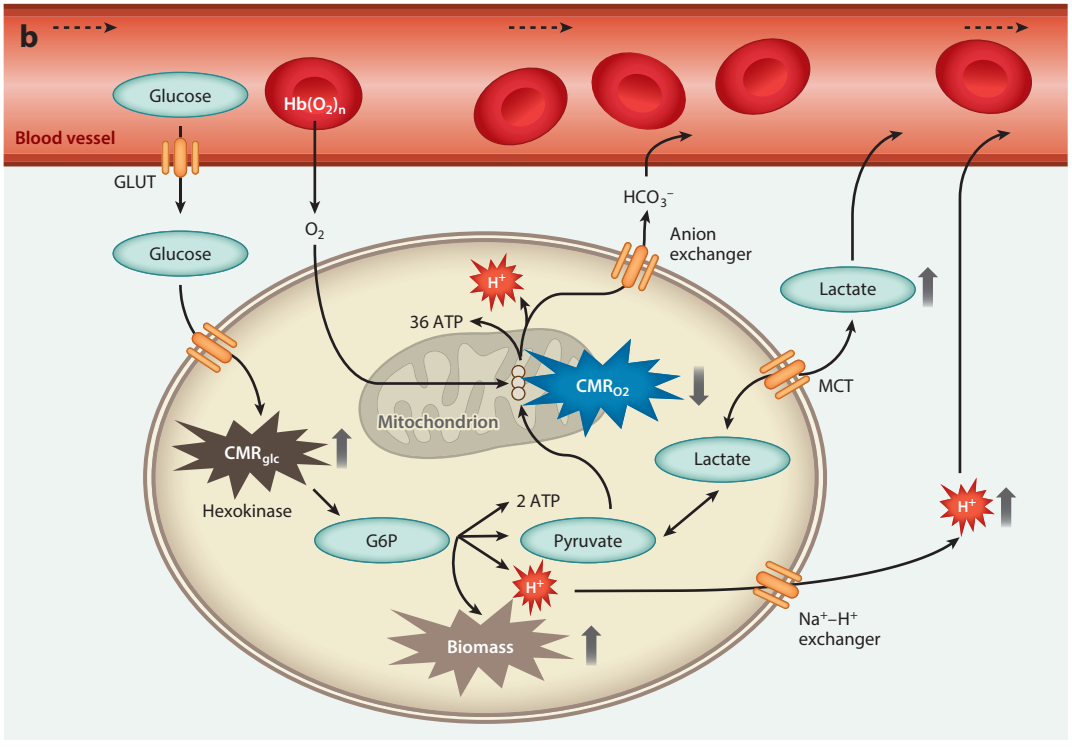
b
Glucose
Hb(O2)n
Blood vessel
GLUT
O2
HCO3−
Anion exchanger
Glucose
H+
36 ATP
CMRO2
Mitochondrion
Lactate
MCT
CMRglc
Hexokinase
Lactate
2 ATP
G6P
Pyruvate
H+
H+
Biomass
Na+–H+ exchanger

plays a central role in glutamatergic and GABAergic synapses [i.e., glutamate is a precursor of GABA, and it is a constituent of both neurons and astrocytes (22)].

Cellular excitability (or signaling) depends on ionic distribution across the cell membrane. For inactive cells, there is an approximately 10-fold difference in ionic distribution between the intracellular and extracellular compartments, with higher concentrations of Na^+, Ca^{2+}, and Cl^- ions outside and a higher but unbalanced concentration of K^+ ions inside. Ion channels on the membrane allow ions to move across it. The concentration gradients and ion channel determine the membrane permeability for each ion; in turn, the membrane permeabilities together determine the membrane voltage. When neurons are excited, the permeability for K^+ and Na^+ increases, resulting in a flip in the polarity of the electrical gradient and inflows of Na^+ and outflows of K^+. The membrane voltage polarity switch can cause the neuron to undergo action potentials (firing) and release neurotransmitters such as glutamate and GABA to, respectively, excite or inhibit other neurons. However, ATP-dependent ion pumps (e.g., Na^+/K^+ ATPase) are needed to help restore the ionic gradients to the resting value, allowing the neuron to fire again.

Communication between neurons is characterized by 1–2-ms epochs of electrical discharge (or depolarization), which are followed by quiescent charging periods lasting a few milliseconds. Repeated discharges, or action potentials, represent neuronal firing (**Figure 2*a***). But synaptic activity is not exclusively mediated by digital (i.e., all or none) signaling alone, because membrane potential changes (i.e., field potentials) are also graded (and slow) to produce analog signals. In contrast to action potentials, the synaptic potentials have a lower amplitude and last several milliseconds (**Figure 2*a***).

Metal microelectrodes enable extracellular recordings of both action and synaptic potentials (**Figure 2*a***). If the tip (1–3 μm) is situated next to cell bodies and the data are collected with high temporal resolution (<100 μs), then the extracellular voltage can be measured to enable multiunit activity (MUA) recordings. The largest signals from neurons closest to the tip are studied, and the signals from others are ignored. The high SNR of action potentials (or spikes) can be distinguished from lower-amplitude signals (by spike sorting). The extracellular signal is also susceptible to the slower waves that represent the local field potential (LFP), which may arise from graded events at the nerve terminal. Thus, appropriate filtering is applied to separate the MUA (10^2–10^3 Hz) from the LFP (<10^2 Hz) signals. MUA signals are typically representative of signals from one or more neurons in the microelectrode's vicinity (spanning 10–100 μm). LFP signals can integrate over much larger distances (micrometers to millimeters) to represent the aggregate activity in that region.

Figure 2

Function of neuronal/glial cells and their energy demand. (*a*) The supply of glucose and oxygen supports the electrical and chemical activities of neurons and astrocytes at the glutamatergic synapse. Extracellular recordings allow measurements of electrical activities represented by multiunit activity (MUA) and local field potential (LFP), whereas a range of magnetic resonance imaging (MRI) and magnetic resonance spectroscopy (MRS) methods are needed to measure the energy demand that support these activities. (*b*) Glucose metabolism in mammalian cells. Blood delivers glucose [through glucose transporters (GLUTs)] and oxygen [from oxyhemoglobin, $Hb(O_2)_n$ (where $4 > n > 1$), by passive diffusion] to tissues. Most of the glucose is converted first to glucose-6-phosphate (G6P) by hexokinase and then to pyruvate and hydrogen ions (H^+), generating two ATP molecules per glucose. In the presence of oxygen, pyruvate is oxidized to form carbon dioxide and water (which is extruded out as HCO_3^-), generating 36 additional ATP molecules per glucose. But some glucose, beyond G6P, is diverted via the pentose phosphate shunt to support biomass. In the absence of oxygen, pyruvate is reduced to lactate. Lactate and H^+ are transported out of the cell by monocarboxylic acid transporter (MCT) and Na^+–H^+ exchanger, respectively. However, uncoupling between glucose metabolism (CMR_{glc}) and oxidative metabolism (CMR_{O2}) in unhealthy (e.g., cancer) cells enhances pathways for biomass and production of lactate and H^+. To maintain intracellular pH homeostasis, both lactate and H^+ are extruded out into the extracellular space to cause acidification.

2.3. A Primer on Brain Metabolism

In no other organ is the continuous energy supply more imperative than in the brain (23). The brain comprises only 2% of the body's weight, but it consumes more than 20% of the oxidative fuels in the entire body and receives nearly as much of the cardiac output to supply nutrients (i.e., glucose and oxygen) (24). Because endogenous energy reserves in the brain—glucose (1–3 mM), oxygen (50–100 μM), glycogen (2–4 mM), and creatine (8–10 mM)—are small (25), normal brain function needs an efficient blood circulation system to provide nutrients to the brain and remove waste generated by the brain (26).

Glucose is the primary energy substrate in the healthy adult brain, although other substrates (e.g., ketone bodies, lipids) can contribute under specific conditions (16). The energetic costs of the brain are met mainly by ATP derived from glucose oxidation, where the ATP yield is ~18 times higher during full oxidation than during glycolysis. Transporters located at both the blood–brain barrier and the plasma membrane mediate glucose delivery. Both nonoxidative and oxidative pathways help break down glucose to maintain a homeostatic level of ATP (2–4 mM). Glucose can be stored in glial cells as glycogen. Because astrocytes lack the enzyme to generate glucose from glycogen, glucose-6-phosphate generated in glia may be transferred to neurons as lactate (27).

Total creatine, which represents both phosphocreatine (PCr) and creatine (Cr), can undergo a phosphorylation–dephosphorylation reaction catalyzed by the cerebral metabolic rate of the creatine kinase (CK) reaction (i.e., CMR_{CK}, which is PCr ↔ ATP + Cr). Therefore, PCr may provide an additional energy reserve when oxidative phosphorylation cannot maintain a constant ATP supply (28). Together, these alternate energy reserves can provide energy support for a short time, for instance, a few minutes under ischemia (4). These extra nonoxidative pathways, most of which are cytosolic, may provide a faster ATP production rate (in the millisecond range) than mitochondrial respiration (27, 28). The unidirectional ATP production rate that is directly related to supporting cellular function by ATP-dependent ion pumps (e.g., Na^+/K^+ ATPase) is the cerebral metabolic rate of ATPase reaction (i.e., CMR_{ATPase}, which is $P_i \rightarrow$ ATP).

Glucose breakdown to pyruvate generates two ATP molecules per glucose molecule, and in the presence of oxygen, pyruvate is fully oxidized to carbon dioxide and water (i.e., glucose + $6O_2 \rightarrow 6CO_2 + 6H_2O$) in the tricarboxylic acid (TCA) cycle, generating 36 additional ATP molecules per glucose molecule (**Figure 2*b***). However, some glucose, beyond glucose-6-phosphate, is diverted to support biomass. When oxygen is lacking, pyruvate is reduced to lactate. Both of these oxidative and nonoxidative processes produce lactate and hydrogen ions (H^+). However, in disease (e.g., cancer), uncoupling of cytosolic glucose metabolism (CMR_{glc}) and mitochondrial oxidative metabolism (CMR_{O2}) enhances pathways for biomass and production of lactate and H^+ (9). To maintain intracellular pH homeostasis, the excess lactate and H^+ generated have to be transported out of the cell, resulting in extracellular acidosis.

To assess regional variations of the ATP utilization rate, the degree of glucose oxidation [$CMR_{glc(ox)}$] must be mapped, as reflected in the oxygen-to-glucose index (OGI),

$$OGI = CMR_{O2}/CMR_{glc}, \quad (1)$$

which can be determined from absolute PET measurements of CMR_{glc} and CMR_{O2} (29, 30).

An OGI lower than six indicates aerobic glycolysis that terminates in generation of lactate (or other metabolites) that remains in the tissue without yielding carbon dioxide and water [i.e., $CMR_{glc(ox)} < CMR_{glc}$]. Conversely, an OGI of six suggests full glucose oxidation [i.e., $CMR_{glc(ox)} = CMR_{glc}$], whereas an OGI greater than six suggests oxidation of other substrates.

3. IMAGING NEUROENERGETICS AND NEUROTRANSMISSION

Physiological studies by Kety and colleagues dating back to the 1950s showed that the active or resting brain has very high CMR_{glc} and CMR_{O2} despite the brain's small size in relation to other organs in the body (24). Despite this disproportionate energy requirement for the brain, prior to the 1990s (and even now, to some extent) investigators believed that the energies devoted to brain function were small (31), suggesting that neuronal activity was essentially negligible at rest compared with the increase in activity measured during sensory stimulation or cognition (32). Recent in vivo ^{13}C-MRS studies in rat and human brain (13) have played an important role in testing these claims and overturning long-held misconceptions about the energetic demand for neural function.

The ability of ^{13}C-MRS to measure the fluxes of the TCA cycle (V_{TCA}) and the total neurotransmitter cycle (V_{cycle}) is due to the localization of key enzymes and metabolite pools in neurons and glia and the specificity of ^{13}C-labeled precursors to specific cell types (33, 34). **Figure 3*a*** shows a diagram of glucose oxidation in neurons ($V_{TCA,N}$) and astrocytes/glia ($V_{TCA,A}$) as well as the interactions between glutamate and GABA neurotransmission and astrocyte metabolism via the glutamate–glutamine cycle ($V_{cycle,Glu/Gln}$) and the GABA–glutamine cycle ($V_{cycle,GABA/Gln}$). Excitatory glutamatergic neurons, which account for 80–90% of the neurons and synapses in the cerebral cortex (1), release glutamate as a neurotransmitter, most of which is taken up by the astrocytes (35) and either converted to glutamine or oxidized (36). Neurons lack the enzymes required for de novo synthesis of glutamate; therefore, they depend on the astrocytes to provide substrates for the synthesis of glutamate lost during neurotransmission (37). The neurons then convert glutamine to glutamate via phosphate-activated glutaminase. In GABAergic neurons, glutamate is converted to GABA through an additional step catalyzed by glutamate decarboxylase.

3.1. ^{13}C-MRS for Tricarboxylic Acid Cycle Flux

Because V_{TCA} is directly related to oxidative phosphorylation (4), in vivo measurements of V_{TCA} are an indicator of mitochondrial health in neurons and glia. **Figure 3*b*** shows two spectra obtained at a B_o value of 4.0 T from human brain localized to the midline occipital parietal lobe during infusions of two different ^{13}C-labeled substrates: [1-^{13}C] glucose and [2-^{13}C] acetate, both enriched to 99% (33). The difference in ^{13}C labeling between [1-^{13}C] glucose and [2-^{13}C] acetate reflects their different pathways of metabolism. Glucose is oxidized primarily in the neuronal TCA cycle, whereas acetate is oxidized first in the astrocyte TCA cycle. As a result, glutamine receives more ^{13}C label when acetate is infused due to it being exclusively synthesized in the astrocyte. These spectra clearly show ^{13}C labeling in the brain pools of aspartate, GABA, glutamine, and glutamate after ~1 h of infusion of the respective substrates. By following the flow of ^{13}C label into these metabolites, ^{13}C-MRS in combination with metabolic modeling enables measurements of V_{TCA} in glutamatergic neurons ($V_{TCA,NGlu}$), GABAergic neurons ($V_{TCA,NGABA}$), and glia ($V_{TCA,A}$), as well as measurements of V_{cycle} for glutamatergic ($V_{cycle,Glu/Gln}$) and GABAergic ($V_{cycle,GABA/Gln}$) neurotransmitter cycles (38).

V_{TCA} determined by ^{13}C-MRS, when expressed as total glucose oxidation [i.e., $CMR_{glc(ox)}$], is in good agreement with earlier PET measurements of CMR_{glc}, assuming an OGI of ~5.3 [i.e., $2\ CMR_{glc(ox)} = V_{TCA}$] (39, 40). V_{TCA} determined by ^{13}C-MRS in rat and human cerebral cortices is also consistent with results using ^{14}C-2-deoxyglucose autoradiography (for CMR_{glc} measurements) and arteriovenous oxygen difference (for CMR_{O2} measurements) (22, 41).

For measurements of $V_{TCA,N}$ and $V_{TCA,A}$, there is good agreement between three independent label strategies using [1-^{13}C] glucose, [2-^{13}C] acetate, and [1-^{13}C] bicarbonate as precursors in

human and animal model studies. In the awake human occipital lobe, 15–20% of substrate oxidation is by glia, and the remaining 70% is by glutamatergic neurons (33). Results in animal models suggest that on the order of 10–20% of cerebral cortex energy consumption may be due to GABAergic neurons (42). In the awake human occipital lobe, $V_{TCA,NGABA}$ was recently estimated to be 10% of $V_{TCA,N}$ (43), consistent with rates of labeling reported in earlier studies (44).

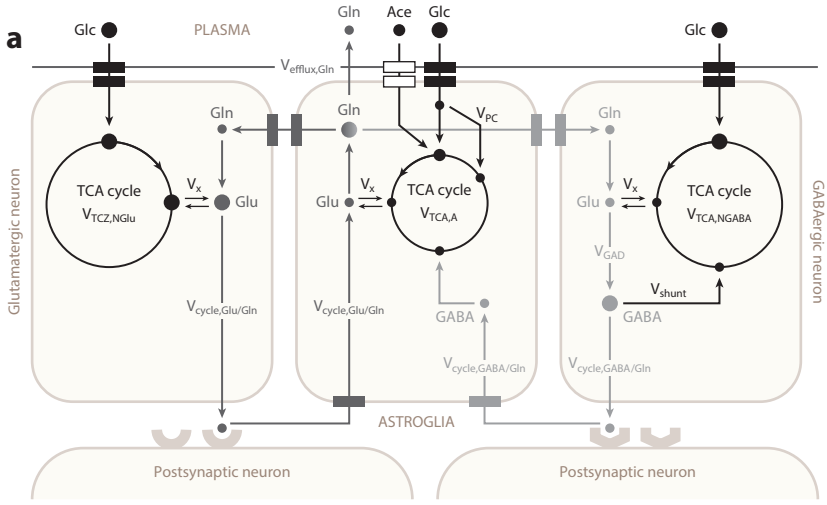

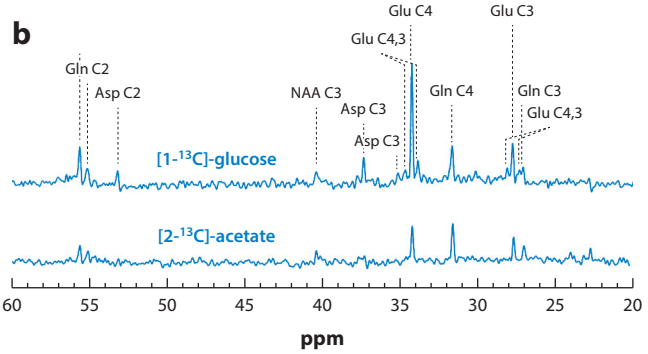

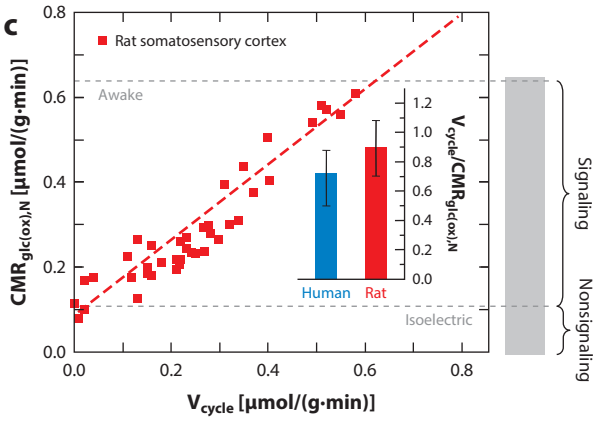

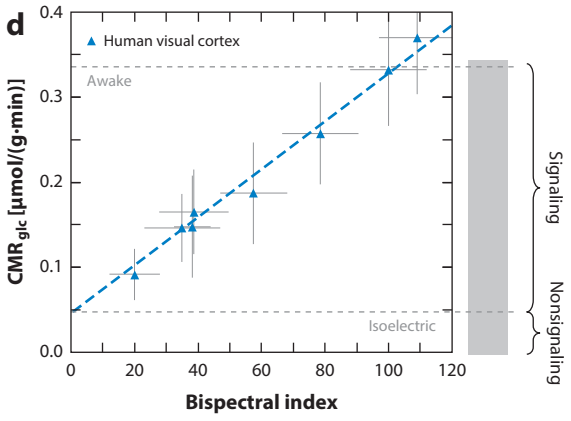

3.2. ^{13}C-MRS for Glutamate Neurotransmitter Flux

Although neuronal signaling is conventionally represented by electrical activity (**Figure 2*a***), noninvasive methods are needed to measure neurotransmission or neuronal activity in people. A potential way to study neurotransmission was suggested by observation of rapid ^{13}C labeling from glucose to glutamate and glutamine in human and animal ^{13}C-MRS studies. The glutamate–glutamine cycle, therefore, is a necessary part of overall cellular excitability but, more importantly, links electrical membrane depolarization to chemical synaptic activity (2, 22). In the cerebral cortex, glutamate released from nerve terminals is taken up by surrounding glial cells and returned to the nerve terminal as glutamine (for details of this process, see Reference 45). If glutamine labeling from the total neurotransmitter cycle, V_{cycle}, could be distinguished from other labeling sources for glutamine (e.g., removal of brain ammonia in the glia by glutamine synthesis), this pathway of glutamatergic neurotransmission could be quantitated by ^{13}C-MRS.

In vivo measurements of V_{cycle} in rat brain were obtained by measuring the increase in the rate of ^{13}C labeling of glutamine (from [1-^{13}C] glucose) as a function of ammonia concentration and then extrapolating to the basal ammonia level (46). As a result of this study, the contribution of de novo glutamine synthesis in the removal of ammonia was estimated to be no more than 10–20%, even in the anesthetized rat cerebral cortex (where metabolic rates are extremely slow compared with the awake state). These early ^{13}C-MRS measurements of V_{cycle} were supported by alternate labeling strategies, with ^{15}N- and ^{13}C-labeled precursors enabling separate and direct measurements of glutamine labeling from both de novo synthesis and the glutamate–glutamine cycle (36, 47). These MRS studies, in conjunction with advanced metabolic modeling (44), support the idea that the glutamate–glutamine cycle accounts for the majority of mass flow into the brain glutamine pool (for a review, see Reference 33).

3.3. Energetics of Signaling and Nonsignaling Components

To address the question of the neuronal energy cost of function, simultaneous ^{13}C-MRS measurements of V_{cycle} and $V_{TCA,N}$ [which is equal to 2 $CMR_{glc(ox),N}$] were conducted for different brain electrical activities (48). ^{13}C-MRS was localized to the rat somatosensory cortex over a wide range of activities, from isoelectric pentobarbital anesthesia, under which there is no neuronal signaling, to mildly anesthetized states with higher neuronal signaling. These earlier ^{13}C-MRS findings

Figure 3

Metabolic measurements from ^{13}C-MRS from normal rat and human brain. (*a*) A four-compartment metabolic model comprising blood plasma, glutamatergic neurons, GABAergic neurons, and astroglia. There are three specific TCA cycle fluxes and two specific neurotransmitter fluxes. (*b*) Localized ^{13}C spectra acquired in a human brain infused with (*top*) [1-^{13}C] glucose and (*bottom*) [2-^{13}C] acetate. (*c*) Relationship between neuronal activity reflected by glutamate neurotransmitter cycling (V_{cycle}; *horizontal axis*) and glucose oxidation in neurons [$CMR_{glc(ox),N}$; *vertical axis*] measured by ^{13}C-MRS in rat brain. The 40 different data points represent a variety of behavioral states—different levels of anesthesia, sleep, seizure, awake, and so forth—from 21 independent studies (see **Supplemental Table 1** and Reference 49 for details). The red line represents the best-fit linear regression (Equation 2a; $R^2 = 0.89$). The V_{cycle}/$CMR_{glc(ox),N}$ ratio in the awake state in rat and human brain (see the studies marked with an asterisk in **Supplemental Table 1** and Reference 49). (*d*) Relationship between BIS representing neuronal activity and glucose consumption (CMR_{glc}) derived by EEG and PET, respectively. The different data points represent a variety of conditions: awake with eyes closed and with eyes open, non–rapid eye movement sleep, halothane, sevoflurane, propofol, acute vegetative, and persistent vegetative (see **Supplemental Table 2** and Reference 49 for details). The dashed blue line represents the best-fit linear regression (Equation 2b; $R^2 = 0.987$). Abbreviations: Ace, acetate; Asp, aspartate; BIS, bispectral index; EEG, electroencephalography; GABA, γ-aminobutyric acid; Glc, glucose; Gln, glutamine; Glu, glutamate; MRS, magnetic resonance spectroscopy; NAA, *N*-acetyl aspartate; PET, positron emission tomography; TCA, tricarboxylic acid. Panel *a* modified from Reference 34 with permission. Panel *b* modified from Reference 33 with permission.

Supplemental Material

Supplemental Material

(48), in good agreement with results from other ^{13}C-MRS experiments in rat brain performed in several laboratories (**Supplemental Table 1**; follow the **Supplemental Material link** from the Annual Reviews home page at **http://www.annualreviews.org**), found a strong coupling between $V_{cycle(tot)}$ versus $CMR_{glc(ox),N}$ (**Figure 3*c***):

$$CMR_{glc(ox),N} = 0.88V_{cycle} + 0.07. \quad (2a)$$

An approximately one-to-one stoichiometric relation between changes in neurotransmission (ΔV_{cycle}) and neuronal energy demand [$\Delta CMR_{glc(ox),N}$] suggests that the oxidative energy required by neurons is a very close surrogate of changes in neuronal activity, where one equivalent of glucose oxidized is accompanied by one equivalent of neurotransmitter glutamate (and GABA) released and recycled. However, at isoelectricity (i.e., when there is no neuronal signaling or when V_{cycle} falls to zero) the remaining $CMR_{glc(ox),N}$ is small but significant [i.e., ~0.1 μmol/(g · min)], equating to ~20% of $CMR_{glc(ox),N}$ in the awake state. Thus, in the awake state ~80% of $CMR_{glc(ox),N}$ is devoted to events associated with signaling and ~20% of $CMR_{glc(ox),N}$ is dedicated to nonsignaling processes, including support for cell housekeeping needs [e.g., (re)building cellular blocks, maintenance of resting membrane potential]. The separation of signaling and nonsignaling energy demands contrasts with prior expectations (see Reference 49 for details).

The ratio of V_{cycle} to $CMR_{glc(ox)N}$ measured in awake human occipital cortex is consistent with findings in rat somatosensory cortex (**Supplemental Table 1**), supporting a similarly high baseline level of neuronal activity (**Figure 3*c***). The slightly lower ratio of V_{cycle} to $CMR_{glc(ox)N}$ in the human studies is probably due to sampling a higher fraction of white matter (where relatively little glutamate neurotransmitter cycling takes place) resulting from the higher percentage of white matter in human brain (50). A recent cortical energy budget found that, in the awake brain, ~80% and ~20% of $CMR_{glc(ox),N}$ are devoted to signaling and nonsignaling components, respectively, in both rats and humans (6). A meta-analysis of electroencephalogram (EEG) and PET data from humans at various levels of activity (**Supplemental Table 2**) shows a linear relationship between total EEG power estimated from the bispectral index (BIS) and CMR_{glc} measured by PET (**Figure 3*d***):

$$CMR_{glc} = 0.003BIS + 0.035. \quad (2b)$$

Here, BIS versus CMR_{glc} has an intercept at ~15% of the resting awake CMR_{glc} value (i.e., when BIS approaches zero), suggesting that in the resting awake human there is a similarly high fraction of energy consumption supporting signaling, as in the rat brain (**Figure 3*c***).

4. IMAGING METABOLIC DEMAND OF RESTING ACTIVITY

Because traditional neuroscientific inquiries have focused largely on neuronal responses evoked by stimuli, the fact that there is a persistent metabolic demand for resting (or baseline) activity had escaped attention. Thus, recent quantitative MRS studies of the resting brain have played a major role in reinvigorating the importance of spontaneous (or resting) activity and its metabolic demand for neuroscientific studies (51).

4.1. ^{31}P-MRS for Rate of ATP Production

Quantitative PET measurements of OGI in normal human brain show globally uniform glucose oxidation in gray matter (~5.3) and white matter (~4.8), but the different OGI values between these tissues suggest that the ATP contribution from glycolytic sources is lower in gray matter than in white matter (52). Whereas the ATP utilization rate can be estimated from PET

measurements of OGI by assuming the efficiency of ATP generated from oxidative phosphorylation (e.g., six ATP molecules per oxygen) and glycolysis (e.g., two ATP molecules per glucose), it is desirable to directly measure ATP synthesis with ^{31}P-MRS (53), a detection scheme that is slightly less sensitive to ^{1}H-MRS (**Table 1**).

Because rates of mitochondrial ATP production and utilization are tightly regulated in normal brain to maintain nearly constant levels of high-energy phosphate compounds (e.g., ATP and PCr) and inorganic phosphate (P_i), measuring their levels does not provide any information about how much ATP is generated versus used (54). In vivo ^{31}P-MRS in conjunction with magnetization transfer (MT) preparation approaches (55) allows simultaneous measurement of two important unidirectional ATP production rates associated with the CK reaction (i.e., CMR_{CK}, which is PCr → ATP) and the ATPase reaction (i.e., CMR_{ATPase}, which is P_i → ATP). The basis for the ^{31}P-MT–MRS experiment is as follows: A significant magnetization (i.e., MRS signal) reduction in the PCr and P_i resonances is observed during steady-state saturation of the ATP resonance, and this MT effect is mediated by CMR_{CK} and CMR_{ATPase}, respectively. The intensity reduction of P_i determines the forward rate constant and flux for the ATPase reaction (i.e., CMR_{ATPase}), whereas the intensity reduction of PCr determines the forward rate constant and flux for the CK reaction (i.e., CMR_{CK}).

Early brain studies using ^{31}P-MT–MRS focused on CMR_{CK} given the higher SNR levels of PCr in the brain (56). But CMR_{ATPase} is directly related to ion pump activity (i.e., Na^+/K^+ ATPase) supporting cellular functions. Recent ^{31}P-MT–MRS studies in normal human brain at a higher B_o value of 7.0 T showed that CMR_{ATPase} can be measured directly by detecting the high SNR P_i resonance during ATP saturation (**Figure 4*a***). A comparison of the reductions in the PCr and P_i resonances observed during ATP saturation shows that CMR_{ATPase} is approximately seven times lower than CMR_{CK} (53, 54). This result suggests that the nonoxidative CK pathway may indeed provide faster ATP (in the millisecond range) than from mitochondrial respiration, reflected by the ATPase reaction (27, 28). These results also show that CMR_{ATPase} is approximately three times higher in gray matter (**Figure 4*a***, *i*) than in white matter (**Figure 4*a***, *ii*). This value agrees with estimates from previous PET and ^{13}C-MRS measurements (22, 52, 57); details of these ^{13}C-MRS measurements are described in Section 3.

4.2. ^{17}O-MRS and ^{19}F-MRS for Oxygen and Glucose Consumption

Recent developments in ^{17}O-MRS and ^{19}F-MRS techniques have enabled measurements of CMR_{O2} (58) and CMR_{glc} (59). Although the very low gyromagnetic ratio and low natural abundance of ^{17}O nucleus seem to suggest poor sensitivity (**Table 1**), the sensitivity of ^{17}O-MRS at higher B_o values is quite comparable to that of ^{1}H-MRS because of the short relaxation times for ^{17}O (i.e., in the millisecond range), allowing for significant signal averaging (60). By contrast, the ^{19}F nucleus has a gyromagnetic ratio that is comparable to that of the ^{1}H nucleus, as well as high natural abundance (**Table 1**). First we describe the principles of ^{19}F-MRS and ^{17}O-MRS, then show how they are used to measure CMR_{glc} and CMR_{O2}, respectively, similarly to the PET techniques (29, 30).

In order to measure CMR_{O2} with ^{17}O-MRS, the amount of water–^{17}O synthesized from inhaled ^{17}O–oxygen (i.e., $^{17}O_2$ → $H_2{}^{17}O$) must be accounted for (versus water–^{17}O recirculated from elsewhere). Because the MRS signal of ^{17}O–oxygen is invisible compared with the MRS signal of water–^{17}O, mitochondrial CMR_{O2} determination is quite direct and less model dependent (60) compared with PET, which requires additional measurements (e.g., CBF by infused water–^{17}O and/or CBV by inhaled carbon monoxide–^{15}O). Recent attempts to measure CMR_{O2} with ^{17}O-MRS in brain used a metabolic model to separate the water–^{17}O generation (and recirculation)

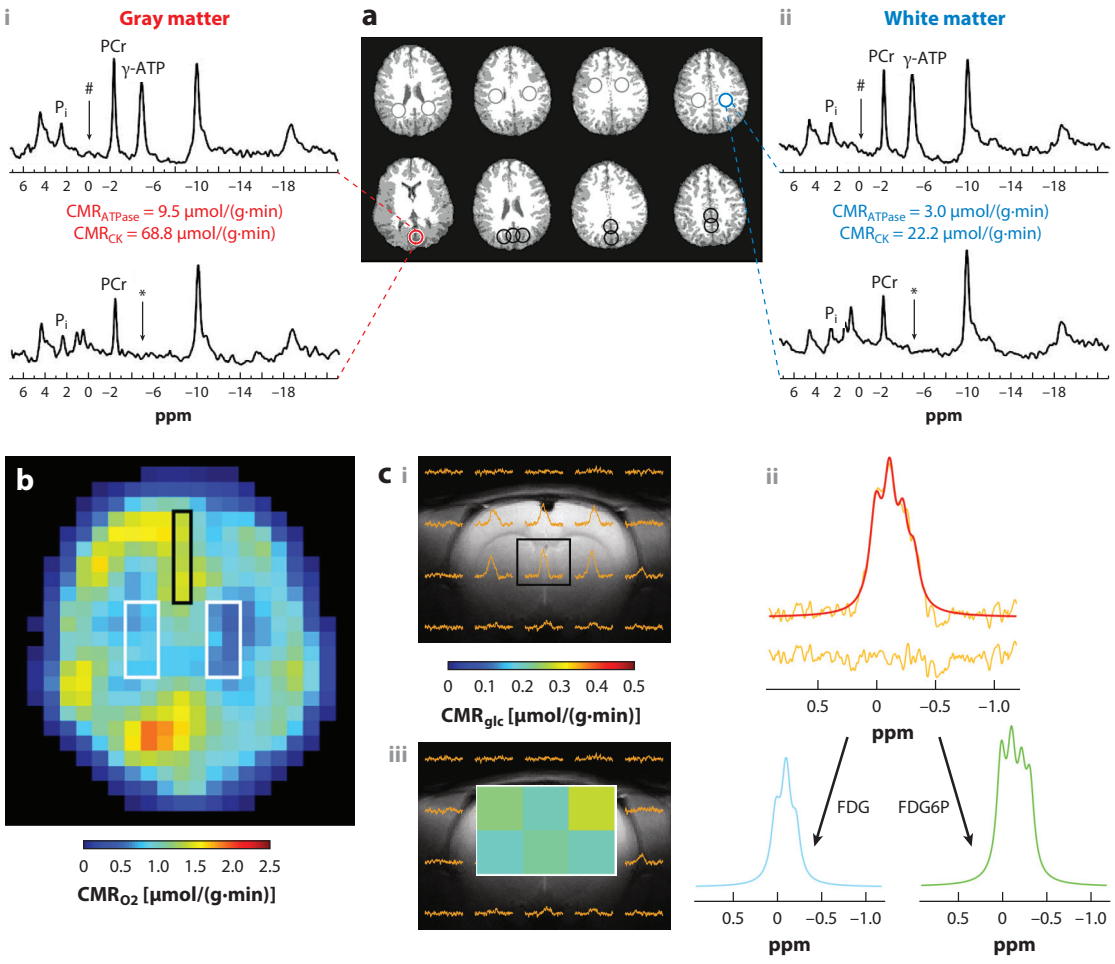

Figure 4

Metabolic measurements from ^{31}P-MRS, ^{17}O-MRS, and ^{19}F-MRS from normal rat and human brain. (*a*) ^{31}P-MRS measurement of ATPase (CMR_{ATPase}) and creatine kinase (CMR_{CK}) rates in (*i*) gray matter (*ii*) and white matter of human brain. ^{31}P-spectra in the absence (pound sign indicates control) and presence (asterisk indicates saturation) of γ-ATP saturation to induce MT. (*b*) ^{17}O-MRS measurement of oxygen consumption (CMR_{O2}) in human brain, revealing significant differences between gray matter [1.42 ± 0.05 μmol/(g · min)] and white matter [0.75 ± 0.11 μmol/(g · min)]. (*c*) ^{19}F-MRS measurement of glucose consumption (CMR_{glc}) in rat brain. (*i*) ^{19}F-spectroscopic image overlaid on MRI. (*ii*) In vivo ^{19}F-spectrum (*brown*) of a voxel (black box in panel *i*) showing separation of ^{19}F-deoxyglucose (^{19}FDG; blue) and ^{19}F-deoxyglucose-6-phosphate synthesized (^{19}FDG6P; green), which upon removal leave a residual signal (*brown*). (*iii*) CMR_{glc} map overlaid on MRI. Abbreviations: MRI, magnetic resonance image; MRS, magnetic resonance spectroscopy; MT, magnetization transfer; PCr; phosphocreatine; P_i, inorganic phosphate. Panel *a* modified from Reference 53 with permission. Panel *b* modified from Reference 61 with permission. Panel *c* modified from Reference 59 with permission.

from water–^{17}O clearance so that the amount of water–^{17}O synthesized from inhaled oxygen–^{17}O could be accurately determined (60–62). In the human brain at a B_o value of 9.4 T, by correcting for regional brain tissue mass, an estimate based on quantitative ^{23}Na-MRS reflecting endogenous tissue Na^+ ions, investigators obtained absolute CMR_{O2} maps by ^{17}O-MRS (**Figure 4*b***) that appear to be in good agreement with absolute CMR_{O2} maps obtained by PET (61).

CMR_{glc} estimation by ^{19}F-MRS involves assessing the trapped ^{19}F-deoxyglucose-6-phosphate (^{19}FDG6P) synthesized from ^{19}F-deoxyglucose (^{19}FDG). Because the MRS signals of ^{19}FDG6P and ^{19}FDG are well separated, cytosolic CMR_{glc} determination by ^{19}F-MRS is easier to interpret (59). In PET estimation of CMR_{glc}, one needs to make specific assumptions about the trapped amount of ^{18}FDG6P versus ^{18}FDG in every voxel [from the lumped constant (24, 29)]. Because FDG competes with glucose for the hexokinase reaction step, it is important to ensure that the FDG dose itself does not compromise the physiological state of the brain tissue.

Past ^{19}F-MRS measurements of FDG and its phosphorylation in the brain have suffered from high dose exposure (63). A recent study showed that a safe FDG dose for rat brain studies can be determined by combining electrophysiological and fMRI measurements to assess the physiological state of the brain (59). In halothane-anesthetized rats, the localized in vivo ^{19}F-MRS detection and separation of FDG and FDG6P signals at a B_o value of 11.7 T showed that CMR_{glc} can be determined (**Figure 4*c***) when assessed in conjunction with a metabolic model based on reversible glucose transport between plasma and brain tissue that includes a nonsaturable plasma-to-tissue component (59). The cortical tissue value of CMR_{glc} by ^{19}F-MRS was in good agreement with the $CMR_{glc(ox)}$ value obtained by ^{13}C-MRS for halothane anesthesia (64).

Quantitative CMR_{glc} and CMR_{O2} measurements are important for understanding the role of metabolism in health and disease (49, 65, 66). Because trace amounts of radioactive tracers are needed for PET measurements, they are easily used for clinical scans. The ^{17}O-MRS method is safe to use clinically, but the high cost of the isotope is prohibitive. Thus far, the ^{19}F-MRS method has been safe in preclinical studies, and it is unlikely to be translated into use in the clinic. Regardless, the combination of ^{17}O-MRS and ^{19}F-MRS in the same experimental setup could be used to assess the role of OGI in a variety of preclinical disease models, specifically in cancer, where rapidly growing tumor cells possess elevated CMR_{glc} rates but reduced CMR_{O2} rates (i.e., the Warburg effect) (9). Given the advent of PET–MRI scanners, combining metabolic PET scans with fMRI (67) and potentially even MRS may provide a metabolic basis for variations in the resting-state networks of the human brain in health and disease.

5. IMAGING METABOLIC DEMAND OF STIMULATED ACTIVITY

The discovery of fMRI has had a great impact on neuroscience. In fMRI, the BOLD contrast is used to expose regions of interest in stimulus-based paradigms. The BOLD contrast arises from the paramagnetic fields generated by deoxyhemoglobin packed inside red blood cells. Because the magnetic properties of changing blood oxygenation (Y) affect the tissue water–^{1}H MRI signal through intravoxel spin dephasing (68), changes in Y are differentially captured with the transverse relaxation rate, as measured by gradient echo (R_2*) and spin echo (R_2). If the relaxation components of R_2* and R_2 assigned to non-susceptibility-based effects are ignored (69), then under well-shimmed conditions their absolute difference yields

$$R_2'(Y) \approx R_2*(Y) - R_2(Y), \qquad (3a)$$

which is the relaxation component that is reversible (e.g., static magnetic field inhomogeneity, slow diffusion regime) (69) and directly measurable (69–73). But how much of the BOLD signal is related to neuronal activity, and therefore related to the energy demand, has been disputed since the earliest days of fMRI (32).

The field of calibrated fMRI emerged from the need to quantitatively measure brain activity with metabolic changes as an index of variation in neuronal activity (**Figure 3*c,d***). By exploiting the CMR_{O2}–CBF and CBV–CBF couplings embedded within the BOLD response ($\Delta S/S$), one

can extract the metabolic component (i.e., $\Delta CMR_{O2}/CMR_{O2}$) (74):

$$\Delta S/S_0 = M\,[1 - (CMR_{O2}/CMR_{O2,0})^{\alpha} CBF/CBF_0)^{\alpha-\beta}]. \quad (3b)$$

Here, the subscript 0 represents the baseline for each parameter, and M represents the maximum baseline BOLD signal and is proportional to $R_2'(Y)$ (69). α describes the CBV–CBF coupling,

$$(CBV/CBV_0) = (CBF/CBF_0)^{\alpha}, \quad (3c)$$

and is assumed to be 0.4 on the basis of PET primate studies with hypercapnia (75); however, α can be directly measured in animals (76, 77), and now in humans (78, 79), by use of intravascular MRI contrast agents based on SPIO nanoparticles. β describes the CMR_{O2}–CBF coupling and ranges between one and two according to the dependence of R_2' on the presence of water diffusion (18):

$$R_2' \propto \nu^{\beta}. \quad (3d)$$

Here, ν accounts for the susceptibility difference between blood and tissue, and the exponent of ν, introduced by Ogawa et al. (18), was termed β by Davis et al. (74). β is assumed to be 1.5 in human studies according to simulations of the BOLD effect at 1.5 T (80), and it is assumed to approach 1 at higher magnetic fields (18). But β can also be directly measured in vivo (81). Calibrated fMRI studies have greatly benefited from MRI methods for CBV and CBF imaging (17, 19).

5.1. Metabolic Demands of Neural Hemodynamic–Associated and –Disassociated Areas

The last decade has witnessed significant advances in calibrated fMRI studies of the human brain (82–84). Preclinical studies allow electrophysiology to be combined with calibrated fMRI so that neurometabolic and neurovascular couplings can be examined (85–91). These studies are helping to answer an important question concerning the metabolic demands of neural hemodynamic–associated and –disassociated areas of the brain (92). The interpretation of regional BOLD responses is contingent on whether LFP and MUA are either disassociated or associated.

In a search for a specific type of neuronal activity that can be visualized by fMRI, Logothetis et al. (93) found that the sensory-evoked BOLD response in primate cerebral cortex is better correlated to LFP than to MUA. Although this result has been used to argue that the cortical BOLD signal reflects primarily LFP, it also implies that MUA is disassociated from LFP. This type of neural hemodynamic disassociation has been reported under a variety of other situations (for a recent review, see Reference 92). Observations of regional dissociation of MUA from LFP, and hence BOLD or CBF, has been rationalized on the basis of both vascular-based and circuitry-based differences. To determine whether neural hemodynamic–associated and –disassociated areas have different metabolic demands, two studies of rat brain at a B_o value of 11.7 T compared sensory-evoked responses of BOLD, CBF, CBV, and CMR_{O2} from the ventral posterolateral thalamic nucleus (VPL) and laminae of the somatosensory forelimb cortex ($S1_{FL}$), and compared these responses to those from MUA and LFP (90, 91).

The rat VPL and $S1_{FL}$ are two model regions in which LFP and MUA can be associated or disassociated from the respective BOLD responses. The capillary density of the thalamus is similar to that of most cortical structures (94). The VPL is composed of star-shaped thalamic cells, which possess closed-field geometry such that synaptic field waveforms may cancel out (95). However, $S1_{FL}$ consists of large populations of pyramidal cells, which are oriented in parallel along the cortex such that synaptic currents integrate and summate (95). The upper $S1_{FL}$ segment consists of neurons projecting to other adjacent cortical areas, the middle $S1_{FL}$ segment contains inputs

from the thalamus and projections to the spinal cord, and the lower $S1_{FL}$ segment has reciprocal connections to and from deeper regions (1, 16).

Forepaw stimulation reproducibly activated the $S1_{FL}$ and VPL, but with different magnitudes of BOLD response (**Figure 5*a***). Layer-specific calibrated fMRI and electrophysiology data in the $S1_{FL}$ during sensory stimulation (**Figure 5*b***) showed that both BOLD and CBV responses decreased from superficial to deep laminae, but these responses were not well correlated with either layer-specific LFP or MUA. However, the CBF changes were quite stable across laminae, similar to LFP. But changes in CMR_{O2} and MUA varied across the cortex in a correlated manner, and both were reduced in the superficial lamina.

Multiregional calibrated fMRI and electrophysiology data in the $S1_{FL}$ (middle segment) and VPL during sensory stimulation (**Figure 5*c***) showed that BOLD and CBV responses were greater in the $S1_{FL}$ than in the VPL, similar to LFP regional differences. Both CBF and CMR_{O2} responses were comparably larger in the $S1_{FL}$ and VPL. Despite different levels of CBF–CMR_{O2} and LFP–MUA couplings in VPL and $S1_{FL}$, CMR_{O2} was well matched with MUA in both regions.

Overall, these results suggest that neural hemodynamic–associated and –disassociated areas in brain can have similar metabolic demands. Therefore, these findings challenge the notion that conventional fMRI can accurately reflect regional changes in neuronal activity unless regionally calibrated.

5.2. Metabolic Interactions Between Resting and Stimulated Activities

Given the prevailing view of the brain as primarily an interactive organ that is active only when stimulated, the consequences of baseline activity are often disregarded (96, 97). If baseline activity were negligible, then the differenced fMRI signal would be a quantitative measure of the neuronal activity induced by a stimulus or task (**Figure 6*a***). However, in the case of high baseline activity, additional assumptions are required in order to assign incremental activity (**Figure 6*a***). Calibrated fMRI is challenging the assumption in cognitive neuroscience that spontaneous (or resting) activity does not interact with task-induced activity, thereby justifying ignoring the baseline signal by differencing or regression (13). However, calibrated fMRI studies show that stimulus-induced changes in brain activity rely on the magnitude of the resting (or baseline) activity (51, 98–101), supporting the idea that there are interactions between spontaneous and evoked activities (i.e., rest–stimulus interactions).

To date, numerous laboratories (58, 85, 87, 102–114), using a variety of neuroimaging techniques applied to different sensory systems, across various species, and under different conditions, have observed that the total neuronal activity reached upon stimulation is, to first order, independent of the level of baseline neuronal activity (98). Their results show that task-induced activity and its commensurate metabolic demand depend on the magnitude of the resting (or baseline) activity and are greater when starting from a lower baseline state (**Figure 6*b–d***). For example, two conditions representing high and low basal states in rat (**Figure 6*b***) and human (**Figure 6*c***) brain showed that different levels of ΔCMR_{O2} reached nearly the same levels of total CMR_{O2}. Moreover, in cat brain, ΔCMR_{O2} is inversely proportional to the magnitude of basal CMR_{O2} (**Figure 6*d***). These findings highlight the danger of ignoring baseline activity, specifically by differencing (100), when interpreting neuroimaging results from fMRI (115).

6. NOVEL METHODS FOR MOLECULAR IMAGING OF CANCER

Rapidly growing tumor cells demonstrate elevated rates of glucose uptake (CMR_{glc}) in relation to oxidative phosphorylation (CMR_{O2}) (116). Gliomas, specifically brain tumors that progress to grade IV glioblastomas (GBMs), are very glycolytic (9). Uncoupling of CMR_{glc} from CMR_{O2},

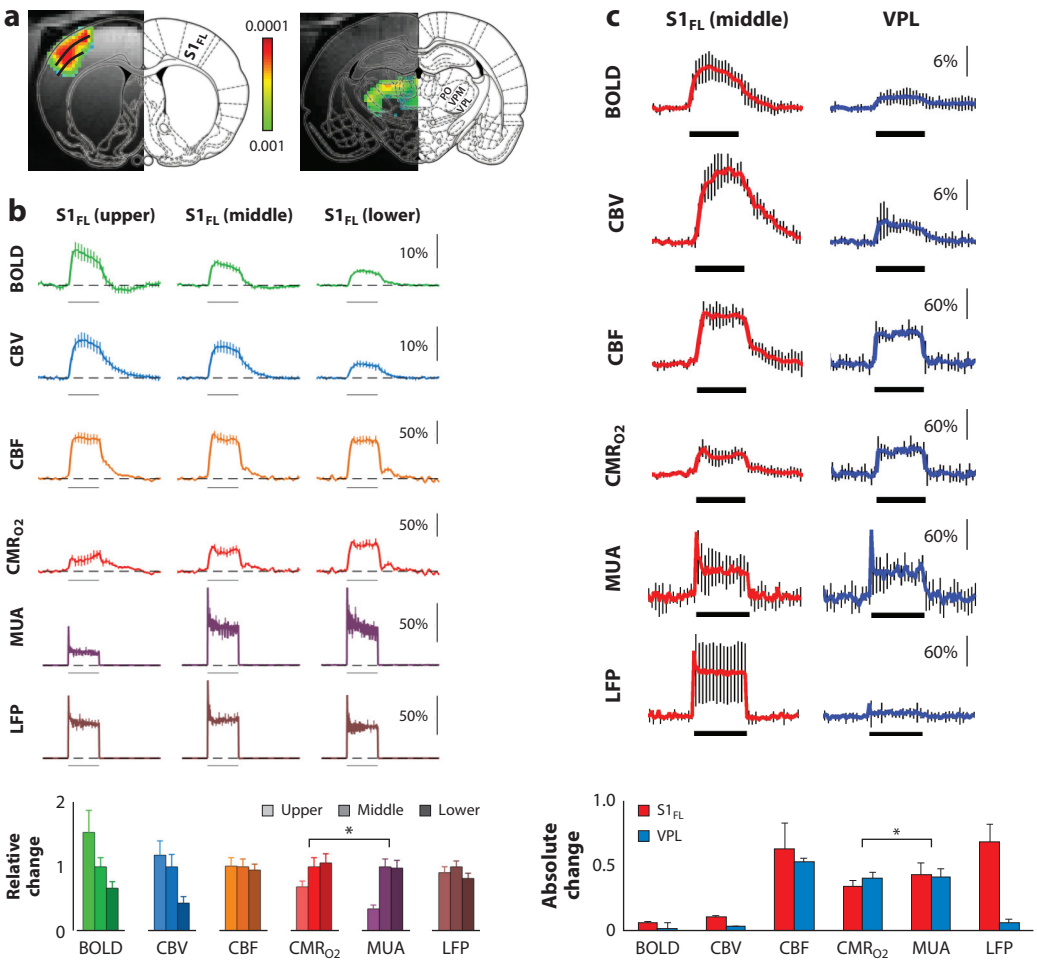

Figure 5

Metabolic demands of neural hemodynamic–associated and neural hemodynamic–disassociated areas in brain. (*a*) Blood oxygenation level–dependent (BOLD) activation maps of the forelimb cortex ($S1_{FL}$) and the thalamus separated into ventral posterolateral thalamic nucleus (VPL), ventral posteromedial nucleus (VPM), and posterior thalamic nuclear complex (PO) obtained during right forepaw stimulation (2 mA, 0.3 ms, 3 Hz) for 30 s (i.e., the horizontal bars in panels *b* and *c*). (*b*) Multimodal responses of BOLD, cerebral blood volume (CBV), cerebral blood flow (CBF), mitochondrial oxidative metabolism (CMR_{O2}), multiunit activity (MUA), and local field potential (LFP) across cortical $S1_{FL}$ laminae (upper, middle, and lower segments, each ~600 μm thick). The horizontal bar represents 30 s of forepaw stimulation. The colored bar chart shows the summary of amplitudes of the multimodal functional responses. All data are shown as mean ± SD (standard deviation). The asterisk indicates that patterns of CMR_{O2} and MUA are quite similar across cortical laminae. (*c*) Multimodal responses of BOLD, CBV, CBF, CMR_{O2}, MUA, and LFP across the cortical $S1_{FL}$ middle laminae and VPL thalamic region. The colored bar chart shows summary of amplitudes of the multimodal functional responses, each normalized by the maximal response to show regional trends. The asterisk indicates that CMR_{O2} and MUA are quite similar between cortical and subcortical regions. All data are shown as mean ± SEM. Panels *a* and *c* modified from Reference 91 with permission. Panel *b* modified from Reference 90 with permission.

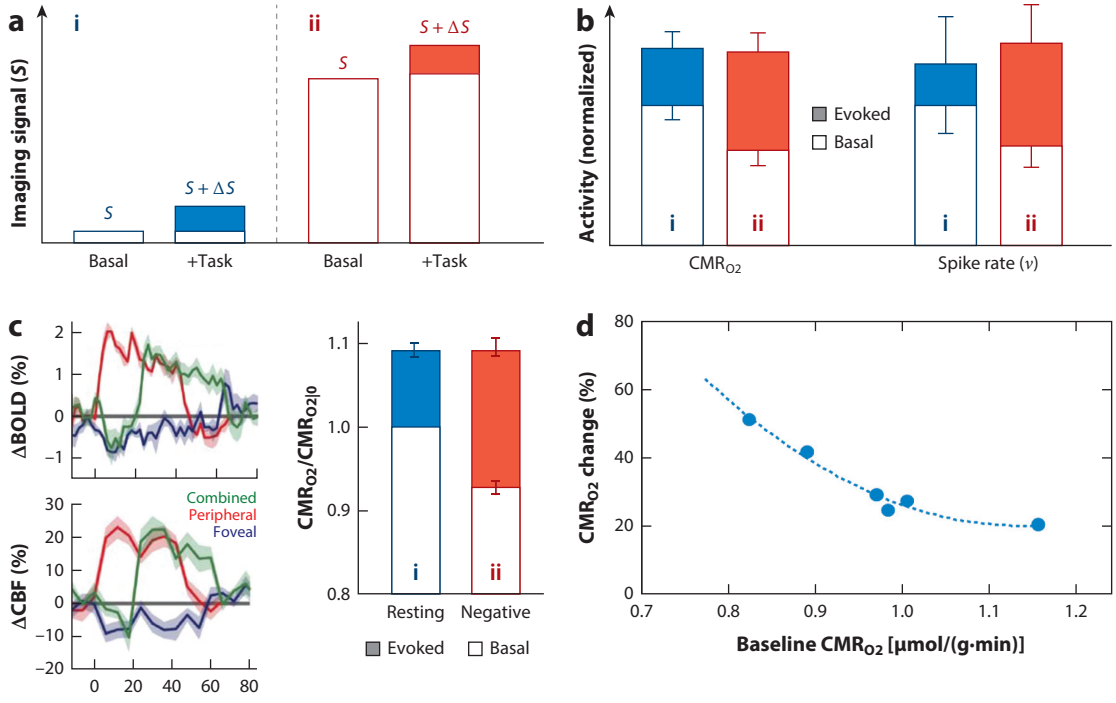

Figure 6

Implications of high basal activity for interpreting functional magnetic resonance imaging (fMRI) data with blood oxygenation level–dependent (BOLD) contrast. (*a*) The neuroimaging signal (*S* in white and Δ*S* shaded) obtained by calibrated fMRI measures CMR_{O2} directly to reflect *S* and *S*+Δ*S* under basal (i.e., no stimuli) and task (i.e., with stimuli) conditions, respectively. (*i*) Δ*S* may be used quantitatively to track task-induced activity in situations of negligible basal activity. (*ii*) Δ*S* cannot be used quantitatively to measure activity needed to support a task in situations of high basal activity. (*b*) In rat somatosensory cortex, the relationship between evoked activity (*shaded*) and basal activity (*white*) is represented by CMR_{O2} (by calibrated fMRI) and neuronal firing (by electrophysiology). Conditions *i* and *ii*, respectively, represent high and low basal states reached by low and high doses of α-chloralose anesthesia. (*c*) In human visual cortex, ΔCMR_{O2} and basal CMR_{O2} are compared using calibrated fMRI. Conditions *i* and *ii*, respectively, represent high and low basal states reached by two different stimuli: peripheral stimulus (induces a positive BOLD response) and foveal stimulus (induces a negative BOLD response). (*d*) In cat visual cortex, ΔCMR_{O2} and basal CMR_{O2} are compared using ^{17}O-MRS (magnetic resonance spectroscopy). Abbreviation: CBF, cerebral blood flow. Panel *b* modified from Reference 85 with permission. Panel *c* modified from Reference 106 with permission. Panel *d* modified from Reference 58 with permission.

otherwise known as aerobic glycolysis (117), enhances pathways for generating biomass and production of excess lactate and H^+ (**Figure 2*b***), which, if not extruded out, can hinder intracellular functions (9). Thus, assessing intracellular pH (pH_i) and/or extracellular pH (pH_e) is important for brain cancer research.

^{31}P-MRS has played an important role in assessing the pH_i–pH_e gradient in a variety of tissues. By measuring protonation level of high-energy phosphate compounds, ^{31}P-MRS can estimate pH_i as follows:

$$pH_i = pK_a + \log\left[(\Delta\delta - \delta_1)/(\delta_2 - \Delta\delta)\right], \quad (4)$$

where $\Delta\delta$ is the shift difference between the P_i and PCr resonances; $\delta_1 = 3.23$ ppm and $\delta_2 = 5.70$ ppm are the corresponding shift differences at low and high pH, respectively; and $pK_a = 6.77$ is the logarithm of the equilibrium constant for the protonating–deprotonating reaction (15). But

pH_e can also be measured by ^{31}P-MRS from the shift of exogenous agents such as 3-aminopropyl phosphonate (3-APP), for which $pK_a = 7.11$, $\delta_1 = 20.34$ ppm, and $\delta_2 = 23.84$ ppm in Equation 4 (118). Previous ^{31}P-MRS studies with 3-APP and P_i showed that inside tumors pH_e is more acidic (6.2–6.9) than pH_i (7.1–7.6) (119–121).

6.1. Intratumoral pH-Weighted Imaging

A new MRI contrast termed chemical exchange saturation transfer (CEST) is generated when an RF pulse (B_1) saturates a pool of exchangeable protons [e.g., amide/amine ($-NH_x$) or hydroxyl ($-OH$) protons] to decrease the steady-state proton signal arising from bulk water (122). CEST contrast from diamagnetic molecules is referred to as diaCEST. B_1 saturation of a pool of exchangeable protons attenuates the proton signal arising from bulk water by

$$S/S_o \approx 1/[1+k_1 T_1], \quad (5)$$

where S and S_o are magnitudes of the bulk water proton signal with and without saturation, k_1 is the pseudo-first-order exchange rate constant, and T_1 is the longitudinal relaxation time of bulk (tissue) water (or is $1/R_1$). For a two-site exchange, k_1 depends on the rate constant of the agent (k_A), concentration of the agent, and number of exchange sites (n). Because k_A and T_1 vary with pH, the CEST effect can reflect the agent's environment, under the assumption that k_A values for different pools are distinct enough to provide specific CEST contrasts (**Figure 7*a***).

Although various diaCEST contrasts can be obtained in theory (123), there are outstanding issues that complicate in vivo diaCEST imaging. Because chemical shifts of the diamagnetic exchangeable protons are within 1–4 ppm of bulk water protons, accounting for off-resonance direct saturation of bulk water and/or macromolecular MT effects from indirect saturation raises concerns about absolute pH quantification from CEST. Moreover there are unknown differences of various parameters [e.g., R_1, temperature, water content, protein content, macromolecular exchange-relayed nuclear Overhauser effects, B_o inhomogeneity, B_1 inhomogeneity] between healthy and diseased tissues. Another critical issue involves accounting for multiple pools that all contribute to the CEST effect simultaneously, as CEST effects of different agents do not follow a general linear model (i.e., $CEST_{A+B} \neq CEST_A + CEST_B$) (124). Nevertheless, the greatest advantage of diaCEST is that it can be clinically applied without any exogenous agent (125).

Amide proton transfer (APT) is a diaCEST contrast generated from proton exchange between protons of bulk water and $-NH_x$ of endogenous mobile proteins and peptides, enabled by saturation at 3.5 ppm downfield of water (**Figure 7*a***). Given that such exchangeable protons (assumed to be arising from endogenous mobile proteins and peptides in the cytoplasm) are more abundant in tumor tissues than in healthy tissues (125), generally a 3–4% APT–CEST contrast increase is observed in the intratumoral region compared with the peritumoral region. Although this APT–CEST contrast increase suggests a pH_i increase, quantitative verification is lacking because the CEST contrast remains qualitative unless the concentration of the exchangeable pool is known. A recent rat study at a B_o value of 7.0 T by Sagiyama et al. (126) used the APT–CEST contrast to monitor the pH_i response of GBM to temozolomide (**Figure 7*b***), which is an oral alkylating chemotherapeutic agent that disturbs DNA replication and induces apoptosis of cancer cells. The APT–CEST contrast for the intratumoral region decreased in tumors 1 week after a single course of treatment, compared with untreated tumors. Because no changes in tumor volume, cell density, or apoptosis were observed in the treated tumors, the authors concluded that the observed change in APT–CEST contrast is due to a pH_i decrease caused by temozolomide.

Amine and amide concentration–independent detection (AACID) is another diaCEST contrast that includes effects from both amine and amide protons in a ratiometric manner such that the

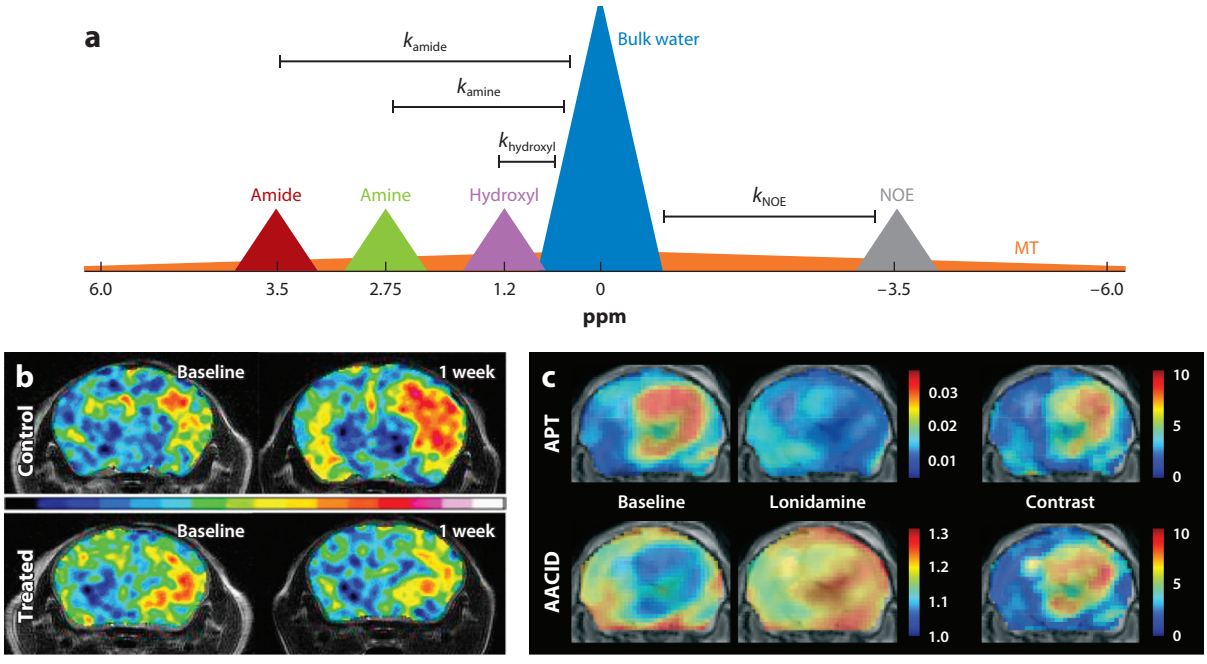

Figure 7

Chemical exchange saturation transfer (CEST) in cancer imaging. (*a*) Illustration of diamagnetic CEST (diaCEST) principles are shown with a schematic diagram of relevant solute exchangeable proton pools (amide, amine, hydroxyl, each with a specific rate constant, k_x; see Equation 5) that resonate at frequencies that are shifted by a few parts per million from that of bulk water proton. However, there are other confounding effects from macromolecular exchange-relayed nuclear Overhauser effects (NOE) and macromolecular magnetization transfer (MT). (*b*) Demonstration of amide proton transfer (APT), which is a diaCEST contrast that depends on amide protons. The rats were either untreated or treated with temozolomide. (*c*) Demonstration of amine and amide concentration–independent detection (AACID), which is another diaCEST contrast that includes effects from both amine and amide protons in a ratiometric manner. The rats were either untreated or treated with lonidamine. Panel *b* modified from Reference 126 with permission. Panel *c* modified from Reference 128 with permission.

need to know the concentration of the exchangeable pool is removed (127). The AACID–CEST contrast is enabled by independent saturations at 2.75 ppm (amine) and 3.5 ppm (amide), both downfield of water (**Figure 7*a***). Whereas the pH_i derived from AACID–CEST contrast can be validated by ^{31}P-MRS, it generates a slightly different (opposite) contrast to that of APT–CEST. A recent rat study at a B_o value of 9.4 T by McVicar et al. (128) compared the AACID–CEST and APT–CEST contrasts to monitor the pH_i response of GBM to lonidamine. Because lonidamine inhibits lactate transport, accumulation of more lactate in the intratumoral region should decrease pH_i compared with the peritumoral region. In agreement with this hypothesis, the APT–CEST contrast in the intratumoral region was lower than in the peritumoral region (**Figure 7*c***). As the APT–CEST contrast is qualitative, the concentration-independent AACID–CEST contrast can be used quantitatively (**Figure 7*c***).

6.2. Intratumoral and Peritumoral pH Imaging

To circumvent some of the drawbacks of diaCEST imaging, a class of paramagnetic cyclen derivatives containing paramagnetic lanthanide (Ln^{3+}) ions, termed paraCEST agents (129), were

synthesized to increase the chemical shift separation between the signals arising from a pool of exchangeable protons in an inner sphere of bound water and bulk solvent water. ParaCEST agents improve CEST contrast by tuning water exchange kinetics (i.e., higher k_1 in Equation 5), chelate structure, and/or choice of Ln^{3+} ion. As US Food and Drug Administration–approved MRI contrast agents containing Gd^{3+} ions that affect bulk (tissue) water R_1 relaxation are based on DOTA (1,4,7,10-tetraazacyclododecane-1,4,7,10-tetraacetic acid), paraCEST agents are also DOTA derivatives, but use other Ln^{3+} ions such as thulium (Tm^{3+}), europium (Eu^{3+}), and so forth. However, in vivo paraCEST imaging has been challenging to perform, primarily because of B_o inhomogeneity issues and the need for high B_1 power (130).

Recently, a new ^{1}H-MRS method termed biosensor imaging of redundant deviation in shifts (BIRDS) was developed. This method uses probes that are similar to paraCEST agents (131–133). Although these BIRDS agents contain exchangeable protons (i.e., $-OH$ and $-NH_x$), the main physiological readout arises from the nonexchangeable protons (i.e., $-CH_y$). Thus, BIRDS combines high–spatial resolution MRI with high molecular specificity MRS into a three-dimensional CSI platform. Because BIRDS agents feature both nonexchangeable and exchangeable protons, both BIRDS and CEST can be carried out with the same probe (134, 135). Unlike the complexity of CEST contrast, with multiple pools of exchangeable protons present (124), a unique feature of BIRDS is that signals from different BIRDS agents follow a general linear model (i.e., $BIRDS_{A+B} = BIRDS_A + BIRDS_B$) (136). Although BIRDS agents use the DOTA framework, clinical use will depend on the use of non-Gd^{3+} ions.

The BIRDS method is based on detection of the agent itself. A ^{1}H spectrum of the chelate (i.e., the compound without the Ln^{3+} ion) shows conventional diamagnetic shifts spanning ~5 ppm (**Figure 8*a***). However, a ^{1}H spectrum of the complexed agent (i.e., the compound with the Ln^{3+} ion) shows paramagnetically shifted resonances more than 100 ppm apart (**Figure 8*b***). These enormously paramagnetically shifted resonances (**Figure 8*c***) have unusual properties because the chelate's nonexchangeable protons are juxtaposed near the paramagnetic field of the metal ion (**Figure 8*c***).

The chemical shift of a BIRDS agent is affected by the proximity of the nuclear spin to the unpaired electrons of the paramagnetic metal ion (137). As a consequence, the relaxation times are severely affected (**Figure 8*c***). The longitudinal ($T_1 = 1/R_1$) and transverse ($T_2 = 1/R_2$) relaxation times of nonexchangeable protons are very short (in the millisecond range), enabling high-resolution, high-speed CSI that is impervious to B_o inhomogeneity. Moreover, BIRDS agents could be used across a range of B_o values because the ratio of T_2 to T_1 remains high and the molecular readout is largely unaffected by B_o. Because the effect on chemical shift depends on the vector L between the spin and unpaired electron(s), the effect of factors such as temperature on L will influence the shift. Similarly, protonation of the complex can alter a molecule's geometry and change the relative shift. Variation of the total shift term, $\Delta\delta_O$, when both temperature (T) and pH change simultaneously, can be modeled as

$$\Delta\delta_O = C_T \Delta T + C_{pH} \Delta pH + C_X \Delta[X], \quad (6)$$

where $C_T = (\Delta\delta_O/\Delta T)_{pH}$ is the temperature dependence at a given pH, $C_{pH} = (\Delta\delta_O/\Delta pH)_T$ is the pH dependence of a given temperature, and the much weaker C_X term is for cation X (**Figure 8*c***). BIRDS characterization depends on C_T and C_{pH} in relation to $\Delta\delta_O$. The molecular readout does not depend on diffusion or blood flow. Although the distribution of BIRDS agents may depend on vessel permeability (e.g., normal versus tumor tissue), the readout is independent of agent dose.

Recent BIRDS studies at a B_o value of 11.7 T, using a pH-sensitive Tm^{3+} probe, measured pH_e in both intratumoral and peritumoral regions of rat brain containing various types of gliomas

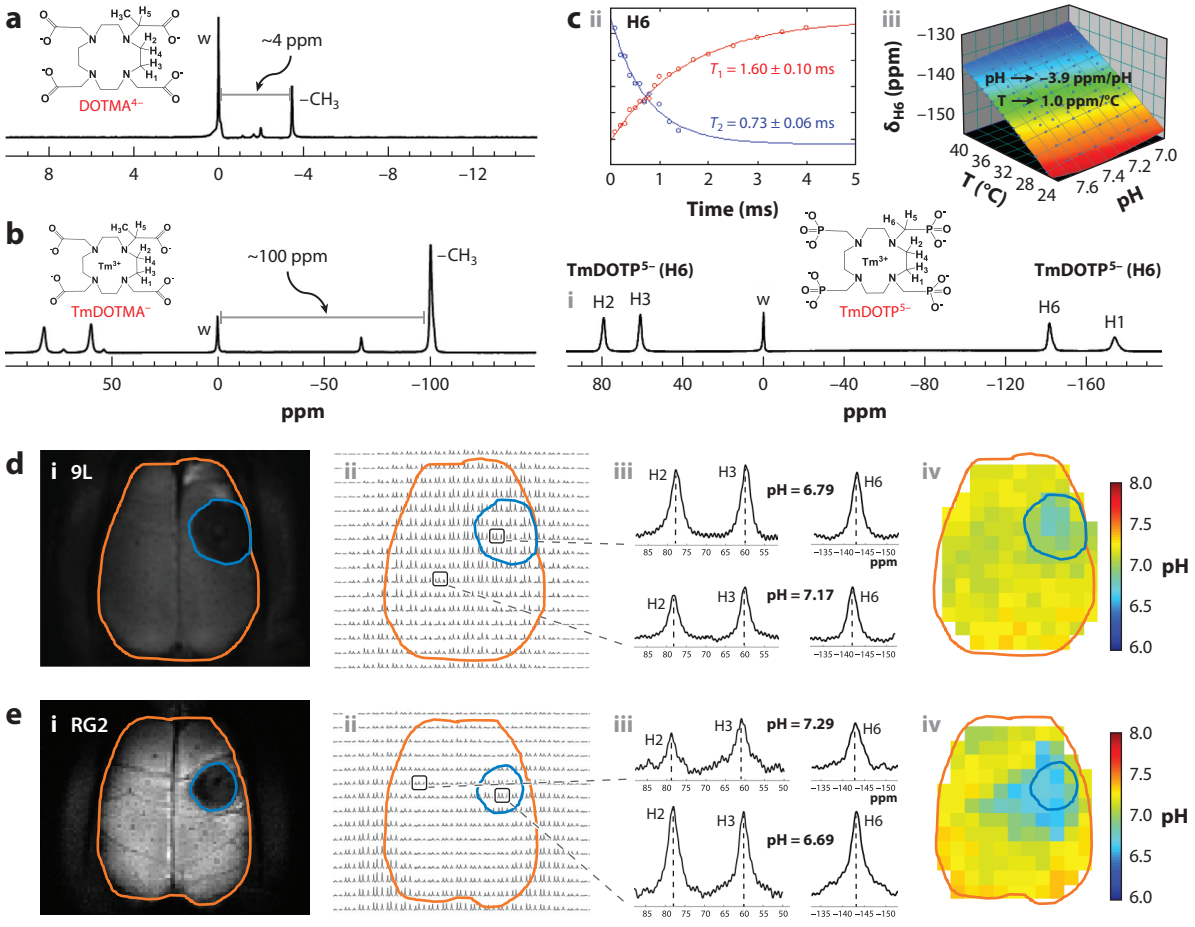

Figure 8

Biosensor imaging of redundant deviation in shifts (BIRDS) in cancer imaging. (*a*) A ^{1}H-spectrum of the chelate [1,4,7,10-tetramethyl 1,4,7,10-tetraazacyclododecane-1,4,7,10-tetraacetate ($DOTMA^{4-}$)] without the paramagnetic thulium ion (Tm^{3+}). (*b*) A ^{1}H-spectrum of the complexed agent with the paramagnetic Tm^{3+} ion ($TmDOTMA^{-}$). (*c*) Properties of a pH-sensitive probe [Tm^{3+} chelated is 1,4,7,10-tetraazacyclododecane-1,4,7,10-tetrakis(methylene phosphonate) ($TmDOTP^{5-}$)]. The paramagnetically shifted ^{1}H resonances are (*i*) more than 100 ppm apart, (*ii*) have very short longitudinal (T_1) and transverse (T_2) relaxation times, and (*iii*) demonstrate shift-dependent temperature (T) and pH sensitivities. (*d*,*e*) Representative extracellular pH (pH_e) maps from BIRDS data of rats bearing (*d*) 9L and (*e*) RG2 tumors. (*i*) T_2-weighted image shows tumor localization (tumor, blue; brain, brown). (*ii*) Chemical shift imaging data for the slice in panel *i* show $TmDOTP^{5-}$ throughout the brain. (*iii*) Examples of spectra from intratumoral and peritumoral voxels. (*iv*) Quantitative pH_e maps from $TmDOTP^{5-}$ peaks and their respective pH sensitivities (Equation 6). Panel *c* modified from Reference 132 with permission. Panels *d* and *e* modified from Reference 138 with permission.

(138, 139). Upon infusion of the BIRDS agent, MRI identified the tumor boundary by enhanced T_2 relaxation (because the Tm^{3+} probe is paramagnetic and affects tissue water T_2), and BIRDS allowed imaging of intratumoral–peritumoral pH_e gradients for different gliomas (138). The pH_e measured by BIRDS was validated by ^{31}P-MRS. Whereas the intratumoral pH_e was acidic for both tumor types, peritumoral pH_e varied with tumor type. The intratumoral–peritumoral pH_e gradient was much larger for the 9L tumor (**Figure 8*c***) than for the RG2 tumor (**Figure 8*d***),

because in the RG2 tumor acidic pH_e was found in distal peritumoral regions. An increased presence of Ki-67$^+$ cells beyond the RG2 tumor border suggested that the RG2 tumor was more invasive than the 9L tumor. These results suggest that intratumoral–peritumoral pH_e gradient mapping is important in monitoring GBM growth and response to treatment.

Because the surgical intervention used to raise the Tm^{3+} probe's plasma concentration (140) limits longitudinal BIRDS scans on the same subject, probenecid (an organic anion transporter inhibitor) can be coinfused with the BIRDS agent to temporarily restrict its renal clearance, thereby facilitating BIRDS without surgical intervention. In vivo BIRDS data using this coinfusion method in rat brain bearing RG2, 9L, and U87 brain tumors showed intratumoral–peritumoral pH_e gradients that were unaffected by the probe dose (139). This coinfusion method can be used for pH_e mapping with BIRDS in preclinical models for tumor characterization and therapeutic monitoring given the possibility of repeated scans with BIRDS (e.g., over days and even weeks) in the same subject. Furthermore, compatibility of BIRDS with various nanoensembles, such as SPIO nanoparticles, liposomes, and even dendrimers (141, 142), may create exciting opportunities for multimodal imaging of drug delivery with MRI (143) and drug response with BIRDS (144).

7. CONCLUDING REMARKS AND FUTURE PERSPECTIVES

In this review, we have discussed advanced MRI and MRS methods that provide a range of options to study how brain metabolism supports functional and nonfunctional processes. The ability to combine these different magnetic resonance methods is already providing unique insights into metabolic changes in health and disease, and we anticipate that this type of research will rapidly expand further. For example, a combination of ^{13}C-MRS and fMRI could provide novel information about degenerative and psychiatric disorders (14, 145–147) and responses to various treatments. Because acidic pH_e favors tumor growth and metastasis by activating matrix metalloproteinases and cathepsins (148) and even drives local tumor cell invasion beyond the tumor core (149), CEST and BIRDS can help assess the efficacy of different GBM treatments by using pH_i and pH_e mapping. Moreover, all of these methods can be performed in combination with more conventional MRI and MRS methods. Our focus on magnetic resonance is not intended to dismiss the importance of other biomedical imaging tools, as the methods utilized should be driven by the questions being asked, given that different methods can provide complimentary information (**Figure 1*a***). For example, a recent study used fMRI to identify brain regions with impaired function in children with dyslexia, and ^{1}H-MRS was used to determine the neurochemical abnormalities underlying these impairments (150). Another recent study found hypofrontality and posterior hyperactivity in a schizophrenia model with fMRI, but this complex impaired functionality was due to anatomical abnormalities in white matter within these regions revealed by DTI; moreover, ^{13}C-MRS showed that these metabolic flux changes underlie the functional alterations in gray matter (14). In the future, combined metabolic and physiological modalities with MRI and MRS could provide a chemical fingerprint for the diagnosis and treatment of a range of degenerative and psychiatric disorders. Although these magnetic resonance methods (e.g., PET combined with MRI/MRS) for imaging brain metabolism demonstrate the translational potential to better diagnose brain disorders and diseases, their combination with other quantitative methods show even greater promise (67).

DISCLOSURE STATEMENT

The authors are not aware of any affiliations, memberships, funding, or financial holdings that might be perceived as affecting the objectivity of this review.

ACKNOWLEDGMENTS

The writing of this review was supported by National Institutes of Health grants R01 MH-067528 (to F.H.), R01 CA-140102 (to F.H.), R01 NS087568 (to D.L.R.), and P30 NS-052519 (to F.H.).

LITERATURE CITED

1. Shepherd GM. 2004. *The Synaptic Organization of the Brain*. New York: Oxford Univ. Press
2. Pereda AE. 2014. Electrical synapses and their functional interactions with chemical synapses. *Nat. Rev. Neurosci.* 15:250–63
3. Kandel ER, Schwartz JH, Jessell TM. 2000. *Principles of Neural Science*. New York: McGraw-Hill
4. Siesjo BK. 1978. *Brain Energy Metabolism*. New York: Wiley
5. Attwell D, Laughlin SB. 2001. An energy budget for signaling in the grey matter of the brain. *J. Cereb. Blood Flow Metab.* 21:1133–145
6. Hyder F, Rothman DL, Bennett MR. 2013. Cortical energy demands of signaling and nonsignaling components in brain are conserved across mammalian species and activity levels. *PNAS* 110:3549–554
7. Bauernfeind AL, Barks SK, Duka T, Grossman LI, Hof PR, Sherwood CC. 2014. Aerobic glycolysis in the primate brain: reconsidering the implications for growth and maintenance. *Brain Struct. Funct.* 219:1149–67
8. Shulman RG, Rothman DL. 1998. Interpreting functional imaging studies in terms of neurotransmitter cycling. *PNAS* 95:11993–98
9. Gatenby RA, Gillies RJ. 2004. Why do cancers have high aerobic glycolysis? *Nat. Rev. Cancer* 4:891–99
10. Mori S, Zhang J. 2006. Principles of diffusion tensor imaging and its applications to basic neuroscience research. *Neuron* 51:527–39
11. Uğurbil K. 2012. The road to functional imaging and ultrahigh fields. *NeuroImage* 62:726–35
12. Huettel SA, Song AW, McCarthy G. 2004. *Functional Magnetic Resonance Imaging*. Sunderland, MA: Sinauer
13. Hyder F, Rothman DL. 2012. Quantitative fMRI and oxidative neuroenergetics. *NeuroImage* 62:985–94
14. Kaneko G, Sanganahalli BG, Groman SM, Wang H, Coman D, et al. 2017. Hypofrontality and posterior hyperactivity in early schizophrenia: multi-modal imaging and behavior in a preclinical model. *Biol. Psychiatry.* 81:503–13. **https://doi.org/10.1016/j.biopsych.2016.05.019**
15. de Graaf RA. 2007. In vivo *NMR Spectroscopy: Principles and Techniques*, Chichester, UK/Hoboken, NJ: Wiley. 2nd ed.
16. Shulman RG, Rothman DL, ed. 2004. *Brain Energetics and Neuronal Activity: Applications to fMRI and Medicine*. New York: Wiley
17. Williams DS, Detre JA, Leigh JS, Koretsky AP. 1992. Magnetic resonance imaging of perfusion using spin inversion of arterial water. *PNAS* 89:212–16
18. Ogawa S, Menon RS, Tank DW, Kim SG, Merkle H, et al. 1993. Functional brain mapping by blood oxygenation level–dependent contrast magnetic resonance imaging. A comparison of signal characteristics with a biophysical model. *Biophys. J.* 64:803–12
19. Kennan RP, Scanley BE, Innis RB, Gore JC. 1998. Physiological basis for BOLD MR signal changes due to neuronal stimulation: separation of blood volume and magnetic susceptibility effects. *Magn. Reson. Med.* 40:840–46
20. Attwell D, Iadecola C. 2002. The neural basis of functional brain imaging signals. *Trends Neurosci.* 25:621–25
21. Nicholls DG. 1989. Release of glutamate, aspartate, and γ-aminobutyric acid from isolated nerve terminals. *J. Neurochem.* 52:331–41
22. Hyder F, Patel AB, Gjedde A, Rothman DL, Behar KL, Shulman RG. 2006. Neuronal–glial glucose oxidation and glutamatergic–GABAergic function. *J. Cereb. Blood Flow Metab.* 26:865–77
23. Aiello LC, Wheeler P. 1995. The expensive-tissue hypothesis—the brain and the digestive system in human and primate evolution. *Curr. Anthropol.* 36:199–221

24. Sokoloff L. 1991. Relationship between functional activity and energy metabolism in the nervous system: whether, where and why? In *Brain Work and Mental Activity*, ed. NA Lassen, DH Ingvar, ME Raichle, L Friberg, pp. 52–64. Copenhagen: Munksgaard
25. Hyder F. 2009. Dynamic imaging of brain function. *Methods Mol. Biol.* 489:3–22
26. Iliff JJ, Lee H, Yu M, Feng T, Logan J, et al. 2013. Brain-wide pathway for waste clearance captured by contrast-enhanced MRI. *J. Clin. Investig.* 123:1299–309
27. Shulman RG, Hyder F, Rothman DL. 2001. Cerebral energetics and the glycogen shunt: neurochemical basis of functional imaging. *PNAS* 98:6417–22
28. Shulman RG, Hyder F, Rothman DL. 2001. Lactate efflux and the neuroenergetic basis of brain function. *NMR Biomed.* 14:389–96
29. Kuwabara H, Gjedde A. 1991. Measurements of glucose phosphorylation with FDG and PET are not reduced by dephosphorylation of FDG-6-phosphate. *J. Nucl. Med.* 32:692–98
30. Ohta S, Meyer E, Thompson CJ, Gjedde A. 1992. Oxygen consumption of the living human brain measured after a single inhalation of positron emitting oxygen. *J. Cereb. Blood Flow Metab.* 12:179–92
31. Creutzfeldt OD. 1975. Neurophysiological correlates of different functional states of the brain. In *Brain Work: The Coupling of Function, Metabolism and Blood Flow in the Brain. Proceedings of the Alfred Benzon Symposium VIII*, ed DH Ingvar, NA Lassen, pp. 21–46. New York: Academic
32. Barinaga M. 1997. What makes brain neurons run? *Science* 276:196–98
33. Rothman DL, De Feyter HM, de Graaf RA, Mason GF, Behar KL. 2011. ^{13}C MRS studies of neuroenergetics and neurotransmitter cycling in humans. *NMR Biomed.* 24:943–57
34. de Graaf RA, Rothman DL, Behar KL. 2011. State of the art direct ^{13}C and indirect ^{1}H-[^{13}C] NMR spectroscopy in vivo. A practical guide. *NMR Biomed.* 24:958–72
35. Bergles DE, Diamond JS, Jahr CE. 1999. Clearance of glutamate inside the synapse and beyond. *Curr. Opin. Neurobiol.* 9:293–98
36. Sibson NR, Mason GF, Shen J, Cline GW, Herskovits AZ, et al. 2001 In vivo ^{13}C NMR measurement of neurotransmitter glutamate cycling, anaplerosis and TCA cycle flux in rat brain during [2-^{13}C]glucose infusion. *J. Neurochem.* 76:975–89
37. Hertz L, Peng L, Dienel GA. 2007. Energy metabolism in astrocytes: high rate of oxidative metabolism and spatiotemporal dependence on glycolysis/glycogenolysis. *J. Cereb. Blood Flow Metab.* 27:219–49
38. Mason GF, Rothman DL. 2004. Basic principles of metabolic modeling of NMR ^{13}C isotopic turnover to determine rates of brain metabolism in vivo. *Metab. Eng.* 6:75–84
39. Boumezbeur F, Besret L, Valette J, Gregoire M-C, Delzescaus T, et al. 2005. Glycolysis versus TCA cycle in the primate brain as measured by combining ^{18}F-FDG PET and ^{13}C-NMR. *J. Cereb. Blood Flow Metab.* 25:1418–23
40. Chaumeil MM, Valette J, Guillermier M, Brouillet E, Boumezbeur F, et al. 2009. Multimodal neuroimaging provides a highly consistent picture of energy metabolism, validating ^{31}P MRS for measuring brain ATP synthesis. *PNAS* 106:3988–93
41. Rothman DL, Behar KL, Hyder F, Shulman RG. 2003. In vivo NMR studies of the glutamate neurotransmitter flux and neuroenergetics: implications for brain function. *Annu. Rev. Physiol.* 65:401–27
42. Patel AB, de Graaf RA, Mason GF, Rothman DL, Shulman RG, Behar KL. 2005. The contribution of GABA to glutamate/glutamine cycling and energy metabolism in the rat cortex in vivo. *PNAS* 102:5588–593
43. Abdallah CG, Jiang L, De Feyter HM, Fasula M, Krystal JH, et al. 2014. Glutamate metabolism in major depressive disorder. *Am. J. Psychiatry* 171:1320–27
44. Gruetter R, Seaquist ER, Uğurbil K. 2001. A mathematical model of compartmentalized neurotransmitter metabolism in the human brain. *Am. J. Physiol. Endocrinol. Metab.* 281:E100–12
45. Rothman DL, Sibson NR, Hyder F, Shen J, Behar KL, Shulman RG. 1999. In vivo nuclear magnetic resonance spectroscopy studies of the relationship between the glutamate–glutamine neurotransmitter cycle and functional neuroenergetics. *Philos. Trans. R Soc. Lond. B* 354:1165–77
46. Sibson NR, Dhankar T, Mason GF, Behar KL, Rothman DL, Shulman RG. 1997. In vivo ^{13}C NMR measurements of cerebral glutamine synthesis as evidence for glutamate–glutamine cycling. *PNAS* 94:2699–704

47. Shen J, Sibson NR, Cline G, Behar KL, Rothman DL, Shulman RG. 1998. ^{15}N-NMR spectroscopy studies of ammonia transport and glutamine synthesis in the hyperammonemic rat brain. *Dev. Neurosci.* 20:434–43
48. Sibson NR, Dhankhar A, Mason GF, Rothman DL, Behar KL, Shulman RG. 1998. Stoichiometric coupling of brain glucose metabolism and glutamatergic neuronal activity. *PNAS* 95:316–21
49. Shulman RG, Hyder F, Rothman DL. 2014. Insights from neuroenergetics into the interpretation of functional neuroimaging: an alternative empirical model for studying the brain's support of behavior. *J. Cereb. Blood Flow Metab.* 34:1721–35
50. Zhang K, Sejnowski TJ. 2000. A universal scaling law between gray matter and white matter of cerebral cortex. *PNAS* 97:5621–26
51. Hyder F, Rothman DL. 2011. Evidence for the importance of measuring total brain activity in neuroimaging. *PNAS* 108:5475–76
52. Hyder F, Herman P, Bailey CJ, Møller A, Globinsky R, et al. 2016. Uniform distributions of glucose oxidation and oxygen extraction in gray matter of normal human brain: no evidence of regional differences of aerobic glycolysis. *J. Cereb. Blood Flow Metab.* 36:903–16
53. Zhu XH, Qiao H, Du F, Xiong Q, Liu X, et al. 2012. Quantitative imaging of energy expenditure in human brain. *NeuroImage* 60:2107–17
54. Du F, Zhu X-H, Zhang Y, Friedman M, Zhang N, et al. 2008. Tightly coupled brain activity and cerebral ATP metabolic rate. *PNAS* 105:6409–14
55. Forsen S, Hoffman RA. 1963. Study of moderately rapid chemical exchange reactions by means of nuclear magnetic double resonance. *J. Chem. Phys.* 39:2892–901
56. Bottomley PA, Hardy CJ. 1992. Proton Overhauser enhancements in human cardiac phosphorus NMR spectroscopy at 1.5 T. *Magn. Reson. Med.* 24:384–90
57. Lin AL, Fox PT, Hardies J, Duong TQ, Gao JH. 2010. Nonlinear coupling between cerebral blood flow, oxygen consumption, and ATP production in human visual cortex. *PNAS* 107:8446–51
58. Zhu XH, Zhang N, Zhang Y, Uğurbil K, Chen W. 2009. New insights into central roles of cerebral oxygen metabolism in the resting and stimulus-evoked brain. *J. Cereb. Blood Flow Metab.* 29:10–18
59. Coman D, Sanganahalli BG, Cheng D, McCarthy T, Rothman DL, Hyder R. 2014. Mapping phosphorylation rate of fluoro-deoxy-glucose in rat brain by ^{19}F chemical shift imaging. *Magn. Reson. Imaging* 32:305–13
60. Zhu XH, Du F, Zhang N, Zhang Y, Lei H, et al. 2009. Advanced in vivo heteronuclear MRS approaches for studying brain bioenergetics driven by mitochondria. *Methods Mol. Biol.* 489:317–57
61. Atkinson IC, Thulborn KR. 2010. Feasibility of mapping the tissue mass corrected bioscale of cerebral metabolic rate of oxygen consumption using 17-oxygen and 23-sodium MR imaging in a human brain at 9.4 T. *NeuroImage* 51:723–33
62. Zhang N, Zhu XH, Lei H, Uğurbil K, Chen W. 2004. Simplified methods for calculating cerebral metabolic rate of oxygen based on ^{17}O magnetic resonance spectroscopic imaging measurement during a short $^{17}O_2$ inhalation. *J. Cereb. Blood Flow Metab.* 24:840–48
63. Nakada T, Kwee IL, Griffey BV, Griffey RH. 1988. ^{19}F 2-FDG NMR imaging of the brain in rat. *Magn. Reson. Imaging* 6:633–35
64. Patel AB, de Graaf RA, Mason GF, Kanamatsu T, Rothman DL, et al. 2004. Glutamatergic neurotransmission and neuronal glucose oxidation are coupled during intense neuronal activation. *J. Cereb. Blood Flow Metab.* 24:972–85
65. Hyder F, Fulbright RK, Shulman RG, Rothman DL. 2013. Glutamatergic function in the resting awake human brain is supported by uniformly high oxidative energy. *J. Cereb. Blood Flow Metab.* 26:865–77
66. Shulman RG, Hyder F, Rothman DL. 2009. Baseline brain energy supports the state of consciousness. *PNAS* 106:11096–101
67. Thompson GJ, Riedl V, Grimmer T, Drzezga A, Herman P, Hyder F. 2016. The whole-brain "global" signal from resting state fMRI as a potential biomarker of quantitative state changes in glucose metabolism. *Brain Connect.* 6:435–47
68. Kennan RP, Zhong J, Gore JC. 1994. Intravascular susceptibility contrast mechanisms in tissues. *Magn. Reson. Med.* 31:9–21

69. Kida I, Kennan RP, Rothman DL, Behar KL, Hyder F. 2000. High-resolution CMR_{O2} mapping in rat cortex: a multiparametric approach to calibration of BOLD image contrast at 7 Tesla. *J. Cereb. Blood Flow Metab.* 20:847–60
70. Kida I, Hyder F, Kennan RP, Behar KL. 1999. Toward absolute quantitation of BOLD functional MRI. *Adv. Exp. Med. Biol.* 471:681–89
71. Hyder F, Kennan RP, Kida I, Mason GF, Behar KL, Rothman DL. 2000. Dependence of oxygen delivery on blood flow in rat brain: a 7 tesla nuclear magnetic resonance study. *J. Cereb. Blood Flow Metab.* 20:485–98
72. Hyder F, Kida I, Behar KL, Kennan RP, Maciejewski PK, Rothman DL. 2001. Quantitative functional imaging of the brain: towards mapping neuronal activity by BOLD fMRI. *NMR Biomed.* 14:413–31
73. Shu CY, Herman P, Coman D, Sanganahalli BG, Wang H, et al. 2016. Brain region and activity-dependent properties of M for calibrated fMRI. *NeuroImage* 125:848–56
74. Davis TL, Kwong KK, Weisskoff RM, Rosen BR. 1998. Calibrated functional MRI: mapping the dynamics of oxidative metabolism. *PNAS* 95:1834–39
75. Grubb RL, Raichle ME, Eichling JO, Ter-Pogossian MM. 1974. The effects of changes in $PaCO_2$ on cerebral blood volume, blood flow, and vascular mean transit time. *Stroke* 5:630–39
76. Keilholz SD, Silva AC, Raman M, Merkle H, Koretsky AP. 2006. BOLD and CBV-weighted functional magnetic resonance imaging of the rat somatosensory system. *Magn. Reson. Med.* 55:316–24
77. Kida I, Rothman DL, Hyder F. 2007. Dynamics of changes in blood flow, volume, and oxygenation: implications for dynamic functional magnetic resonance imaging calibration. *J. Cereb. Blood Flow Metab.* 27:690–96
78. Qiu D, Zaharchuk G, Christen T, Ni WW, Moseley ME. 2012. Contrast-enhanced functional blood volume imaging (CE-fBVI): enhanced sensitivity for brain activation in humans using the ultrasmall superparamagnetic iron oxide agent ferumoxytol. *NeuroImage* 62:1726–31
79. Christen T, Pannetier NA, Ni WW, Qiu D, Moseley ME, et al. 2014. MR vascular fingerprinting: a new approach to compute cerebral blood volume, mean vessel radius, and oxygenation maps in the human brain. *NeuroImage* 89:262–70
80. Boxerman JL, Hamberg LM, Rosen BR, Weisskoff RM. 1995. MR contrast due to intravascular magnetic susceptibility perturbations. *Magn. Reson. Med.* 34:555–66
81. Shu CY, Sanganahalli BG, Coman D, Herman P, Rothman DL, Hyder F. 2016. Quantitative β mapping for calibrated fMRI. *NeuroImage* 126:219–28
82. Hoge RD. 2012. Calibrated fMRI. *NeuroImage* 62:930–37
83. Pike GB. 2012. Quantitative functional MRI: concepts, issues and future challenges. *NeuroImage* 62:1234–40
84. Buxton RB. 2012. Dynamic models of BOLD contrast. *NeuroImage* 62:953–61
85. Smith AJ, Blumenfeld H, Behar KL, Rothman DL, Shulman RG, Hyder F. 2002. Cerebral energetics and spiking frequency: the neurophysiological basis of fMRI. *PNAS* 99:10765–70
86. Kida I, Smith AJ, Blumenfeld H, Behar KL, Hyder F. 2006. Lamotrigine suppresses neurophysiological responses to somatosensory stimulation in the rodent. *NeuroImage* 29:216–24
87. Maandag NJ, Coman D, Sanganahalli BG, Herman P, Smith AJ, et al. 2007. Energetics of neuronal signaling and fMRI activity. *PNAS* 104:20546–51
88. Sanganahalli BG, Herman P, Blumenfeld H, Hyder F. 2009. Oxidative neuroenergetics in event-related paradigms. *J. Neurosci.* 29:1707–18
89. Herman P, Sanganahalli BG, Hyder F. 2009. Multimodal measurements of blood plasma and red blood cell volumes during functional brain activation. *J. Cereb. Blood Flow Metab.* 29:19–24
90. Herman P, Sanganahalli BG, Blumenfeld H, Rothman DL, Hyder F. 2013. Quantitative basis for neuroimaging of cortical laminae with calibrated functional MRI. *PNAS* 110:15115–20
91. Sanganahalli BG, Herman P, Rothman DL, Blumenfeld H, Hyder F. 2016. Metabolic demands of neural-hemodynamic associated and disassociated areas in brain. *J. Cereb. Blood Flow Metab.* 36:1695–707
92. Ekstrom A. 2010. How and when the fMRI BOLD signal relates to underlying neural activity: the danger in dissociation. *Brain Res. Rev.* 62:233–44
93. Logothetis NK, Pauls J, Augath M, Trinath T, Oeltermann A. 2001. Neurophysiological investigation of the basis of the fMRI signal. *Nature* 412:150–57

94. Borowsky IW, Collins RC. 1989. Metabolic anatomy of brain: a comparison of regional capillary density, glucose metabolism, and enzyme activities. *J. Comp. Neurol.* 288:401–13
95. Mitzdorf U. 1985. Current source–density method and application in cat cerebral cortex: investigation of evoked potentials and EEG phenomena. *Physiol. Rev.* 65:37–100
96. Stark CE, Squire LR. 2001. When zero is not zero: the problem of ambiguous baseline conditions in fMRI. *PNAS* 98:12760–66
97. Morcom AM, Fletcher PC. 2007. Does the brain have a baseline? Why we should be resisting a rest. *NeuroImage* 37:1073–82
98. Hyder F, Rothman DL, Shulman RG. 2002. Total neuroenergetics support localized brain activity: implications for the interpretation of fMRI. *PNAS* 99:10771–76
99. Shulman RG, Rothman DL, Hyder F. 1999. Stimulated changes in localized cerebral energy consumption under anesthesia. *PNAS* 96:3245–50
100. Shulman RG, Rothman DL, Hyder F. 2007. A BOLD search for baseline. *NeuroImage* 36:277–81
101. Northoff G, Duncan NW, Hayes DJ. 2010. The brain and its resting state activity—experimental and methodological implications. *Prog. Neurobiol.* 92:593–600
102. Portas CM, Krakow K, Allen P, Josephs O, Armony JL, Frith CD. 2000. Auditory processing across the sleep–wake cycle: simultaneous EEG and fMRI monitoring in humans. *Neuron* 28:991–99
103. Uludağ K, Dubowitz DJ, Yoder EJ, Restom K, Liu TT, Buxton RB. 2004. Coupling of cerebral blood flow and oxygen consumption during physiological activation and deactivation measured with fMRI. *NeuroImage* 23:148–55
104. Chen LM, Friedman RM, Roe AW. 2005. Optical imaging of SI topography in anesthetized and awake squirrel monkeys. *J. Neurosci.* 25:7648–59
105. Masamoto K, Kim T, Fukuda M, Wang P, Kim SG. 2007. Relationship between neural, vascular, and BOLD signals in isoflurane-anesthetized rat somatosensory cortex. *Cereb. Cortex* 17:942–50
106. Pasley BN, Inglis BA, Freeman RD. 2007. Analysis of oxygen metabolism implies a neural origin for the negative BOLD response in human visual cortex. *NeuroImage* 36:269–76
107. Issa EB, Wang X. 2008. Sensory responses during sleep in primate primary and secondary auditory cortex. *J. Neurosci.* 28:14467–80
108. Issa EB, Wang X. 2009. Altered neural responses to sounds in primate primary auditory cortex during slow-wave sleep. *J. Neurosci.* 31:2965–73
109. Li A, Gong L, Xu F. 2011. Brain-state-independent neural representation of peripheral stimulation in rat olfactory bulb. *PNAS* 108:5087–92
110. Crochet S, Petersen CC. 2006. Correlating whisker behavior with membrane potential in barrel cortex of awake mice. *Nat. Neurosci.* 9:608–10
111. Kroeger D, Amzica F. 2007. Hypersensitivity of the anesthesia-induced comatose brain. *J. Neurosci.* 27:10597–607
112. Murayama M, Larkum ME. 2009. Enhanced dendritic activity in awake rats. *PNAS* 106:20482–86
113. Civillico EF, Contreras D. 2012. Spatiotemporal properties of sensory responses in vivo are strongly dependent on network context. *Front. Syst. Neurosci.* 6:25
114. Sellers KK, Bennett DV, Hutt A, Williams JH, Frohlich F. 2015. Awake versus. anesthetized: layer-specific sensory processing in visual cortex and functional connectivity between cortical areas. *J. Neurophysiol.* 113:3798–815
115. Hyder F, Herman P, Sanganahalli BG, Coman D, Blumenfeld H, Rothman DL. 2011. Role of ongoing, intrinsic activity of neuronal populations for quantitative neuroimaging of functional magnetic resonance imaging–based networks. *Brain Connect.* 1:185–93
116. Warburg O. 1956. On the origin of cancer cells. *Science* 123:309–14
117. Lunt SY, Vander Heiden MG. 2011. Aerobic glycolysis: meeting the metabolic requirements of cell proliferation. *Annu. Rev. Cell Dev. Biol.* 27:441–64
118. Gillies RJ, Liu Z, Bhujwalla Z. 1994. ^{31}P-MRS measurements of extracellular pH of tumors using 3-aminopropylphosphonate. *Am. J. Physiol. Cell Physiol.* 267:C195–203
119. Bhujwalla ZM, Artemov D, Ballesteros P, Cerdan S, Gillies RJ, Solaiyappan M. 2002. Combined vascular and extracellular pH imaging of solid tumors. *NMR Biomed.* 15:114–19

120. Raghunand N, Altbach MI, van Sluis R, Baggett B, Taylor CW, et al. 1999. Plasmalemmal pH gradients in drug-sensitive and drug-resistant MCF-7 human breast carcinoma xenografts measured by ^{31}P magnetic resonance spectroscopy. *Biochem. Pharmacol.* 57:309–12
121. Gillies RJ. 2001. The tumour microenvironment: causes and consequences of hypoxia and acidity. Introduction. *Novartis Found Symp*. 240:1–6
122. Ward KM, Balaban RS. 2000. Determination of pH using water protons and chemical exchange dependent saturation transfer (CEST). *Magn. Reson. Med.* 44:799–802
123. van Zijl PC, Yadav NN. 2011. Chemical exchange saturation transfer (CEST): What is in a name and what isn't? *Magn. Reson. Med.* 65:927–48
124. Woessner DE, Zhang S, Merritt ME, Sherry AD. 2005. Numerical solution of the Bloch equations provides insights into the optimum design of PARACEST agents for MRI. *Magn. Reson. Med.* 53:790–99
125. Zhou J, Lal B, Wilson DA, Laterra J, van Zijl PC. 2003. Amide proton transfer (APT) contrast for imaging of brain tumors. *Magn. Reson. Med.* 50:1120–26
126. Sagiyama K, Mashimo T, Togao O, Vemireddy V, Hatanpaa KJ, et al. 2014. In vivo chemical exchange saturation transfer imaging allows early detection of a therapeutic response in glioblastoma. *PNAS* 111:4542–547
127. McVicar N, Li AX, Gonçalves DF, Bellyou M, Meakin SO, et al. 2014. Quantitative tissue pH measurement during cerebral ischemia using amine and amide concentration–independent detection (AACID) with MRI. *J. Cereb. Blood Flow Metab.* 34:690–98
128. McVicar N, Li AX, Meakin SO, Bartha R. 2015. Imaging chemical exchange saturation transfer (CEST) effects following tumor-selective acidification using Ionidamine. *NMR Biomed*. 28:566–75
129. Sherry AD, Woods M. 2008. Chemical exchange saturation transfer contrast agents for magnetic resonance imaging. *Annu. Rev. Biomed. Eng*. 10:391–411
130. Sheth VR, Li Y, Chen LQ, Howison CM, Flask CA, Pagel MD. 2012. Measuring in vivo tumor pHe with CEST-FISP MRI. *Magn. Reson. Med.* 67:760–68
131. Coman D, Trubel HK, Rycyna RE, Hyder F. 2009. Brain temperature and pH measured by ^{1}H chemical shift imaging of a thulium agent. *NMR Biomed*. 22:229–39
132. Coman D, Trubel HK, Hyder F. 2010. Brain temperature by biosensor imaging of redundant deviation in shifts (BIRDS): comparison between $TmDOTP^{5-}$ and $TmDOTMA^{-}$. *NMR Biomed*. 23:277–85
133. Coman D, de Graaf RA, Rothman DL, Hyder F. 2013. In vivo 3D molecular imaging with BIRDS at high spatiotemporal resolution. *NMR Biomed*. 26:1589–95
134. Coman D, Kiefer GE, Rothman DL, Sherry AD, Hyder F. 2011. A lanthanide complex with dual biosensing properties: CEST (chemical exchange saturation transfer) and BIRDS (biosensor imaging of redundant deviation in shifts) with europium DOTA-tetraglycinate. *NMR Biomed*. 24:1216–25
135. Huang Y, Coman D, Kiefer GE, Samuel S, Hyder F. 2013. Multivalent imaging with a cocktail of PARACEST agents: utility of BIRDS for CEST imaging. *Proc. Int. Soc. Mag. Reson. Med.* 21:4218
136. Huang Y, Coman D, Ali MM, Hyder F. 2015. Lanthanide ion (III) complexes of 1,4,7,10-tetraazacyclododecane-1,4,7,10-tetraaminophosphonate for dual biosensing of pH with chemical exchange saturation transfer (CEST) and biosensor imaging of redundant deviation in shifts (BIRDS). *Contrast Media Mol. Imaging* 10:51–58
137. Abragam A. 1961. *Principles of Nuclear Magnetism*. Oxford, UK: Oxford Univ. Press
138. Coman D, Huang Y, Rao JU, De Feyter HM, Rothman DL, et al. 2016. Imaging the intratumoral–peritumoral extracellular pH gradient of gliomas. *NMR Biomed*. 29:309–19
139. Huang Y, Coman D, Herman P, Rao J, Maritim S, Hyder F. 2016. Towards longitudinal mapping of extracellular pH in gliomas. *NMR Biomed*. 29:1364–72
140. Trubel HK, Maciejewski PK, Farber JH, Hyder F. 2003. Brain temperature measured by ^{1}H-NMR in conjunction with a lanthanide complex. *J. Appl. Physiol.* 94:1641–49
141. Maritim S, Huang Y, Coman D, Hyder F. 2014. Characterization of a lanthanide complex encapsulated with MRI contrast agents into liposomes for biosensor imaging of redundant deviation in shifts (BIRDS). *J. Biol. Inorg. Chem.* 19:1385–98
142. Huang Y, Coman D, Hyder F, Ali MM. 2015. Dendrimer-based responsive MRI contrast agents (G1–G4) for biosensor imaging of redundant deviation in shifts (BIRDS). *Bioconjug. Chem.* 26:2315–23

143. Strohbehn G, Coman D, Han L, Ragheb RR, Fahmy TM, et al. 2015. Imaging the delivery of brain-penetrating PLGA nanoparticles in the brain using magnetic resonance. *J. Neurooncol.* 121:441–49
144. Coman D, Sanganahalli BG, Jiang L, Hyder F, Behar KL. 2015. Distribution of temperature changes and neurovascular coupling in rat brain following 3,4-methylenedioxymethamphetamine (MDMA, "ecstasy") exposure. *NMR Biomed.* 28:1257–66
145. Boumezbeur F, Mason GF, de Graaf RA, Behar KL, Cline GW, et al. 2010. Altered brain mitochondrial metabolism in healthy aging as assessed by in vivo magnetic resonance spectroscopy. *J. Cereb. Blood Flow Metab.* 30:211–21
146. Lin AL, Coman D, Jiang L, Rothman DL, Hyder F. 2014. Caloric restriction impedes age-related decline of mitochondrial function and neuronal activity. *J. Cereb. Blood Flow Metab.* 34:1440–43
147. Sanganahalli BG, Herman P, Behar KL, Blumenfeld H, Rothman DL, Hyder F. 2013. Functional MRI and neural responses in a rat model of Alzheimer's disease. *NeuroImage* 79:404–11
148. Hashim AI, Zhang X, Wojtkowiak JW, Martinez GV, Gillies RJ. 2011. Imaging pH and metastasis. *NMR Biomed.* 24:582–91
149. Estrella V, Chen T, Lloyd M, Wojtkowiak J, Cornnell HH, et al. 2013. Acidity generated by the tumor microenvironment drives local invasion. *Cancer Res.* 73:1524–35
150. Pugh KR, Frost SJ, Rothman DL, Hoeft F, Del Tufo SN, et al. 2014. Glutamate and choline levels predict individual differences in reading ability in emergent readers. *J Neurosci.* 43:4082–89